Initial data for the black hole plus Brill wave spacetime

David Bernstein,[1,*] David Hobill,[1,2] Edward Seidel,[1]
and Larry Smarr[1]
[1]*National Center for Supercomputing Applications, 605 E. Springfield Avenue Champaign, Illinois 61820*
[2]*Department of Physics and Astronomy, University of Calgary, Calgary, Alberta, Canada T2N 1N4*
(Received 25 March 1994)

In this paper we present a new initial data set for use in numerical relativity investigations involving black-hole–gravitational-wave interactions. The initial data are time symmetric and are constructed on a spacelike hypersurface with the topology of a single Einstein-Rosen bridge ($\mathbf{S}^2 \times \mathbf{R}$). The two "sheets" of the bridge are chosen to be isometric through a two-sphere and this requires the two-sphere to be a marginally trapped surface. The three-metric is in the form used by Brill and others to study time symmetric gravitational waves, the form of the wave being chosen to maintain this isometry. There are three parameters which control the amplitude, width, and range of the wave from the isometry surface. Various physical results are determined as a function of these parameters including the mass of the slice, the geometry of various two-surfaces within the slice, the location and geometry of apparent horizons, and the form of curvature and radiation quantities traditionally used in numerical relativity calculations. We also present a linearized analysis of the data sets.

PACS number(s): 04.20.Ex, 04.25.Dm

I. INTRODUCTION

An often stated goal of numerical relativity is the computation of the fully three-dimensional spiral infall and collision of two black holes. Progress toward this goal began in the middle 1960s with the work of Hahn and Lindquist [1] on the radial infall and collision of two holes (known colloquially as "the two black hole spacetime"). Despite the maturation of numerical relativity as a field in the intervening 30 years, the fully relativistic spiral infall problem has not been attempted, and there remains a significant amount of work to be done in the physics, mathematics, and numerical algorithms needed to understand the complete nature of the problem. Today the urgency of computing the solution to the Einstein equations corresponding to the spiral infall of two concentrated bodies is made greater by the construction of the Laser Interferometric Gravitational Wave Observatory (LIGO) [2], the first gravitational wave detector likely to observe such an event. The purpose of this paper and its companions is to describe a spacetime which may be considered as a "simple case" in the numerical construction of purely vacuum spacetimes containing very distorted black holes. Such a spacetime is useful both as a proving ground for numerical algorithms and as a tool for honing our intuition about dynamic black holes.

In spirit this work follows the pioneering efforts of Hahn and Lindquist, Čadež, Smarr, and Eppley on the two black hole spacetime [1,3–5] and the work of Eppley, Miyama, and Abrahams and Evans on the pure Brill wave spacetime [6–9]. In the former we have two black holes, created by two Einstein-Rosen bridges, colliding from an initial moment of time symmetry, in the latter we have the implosion and radiation of gravitational waves in an otherwise empty spacetime. Both spacetimes contain strongly time-dependent gravitational fields and (possibly in the latter case) black holes. The black hole plus Brill wave spacetime contains one hole, formed by one bridge, surrounded by a cloud of gravitational radiation of variable intensity. It therefore occupies a niche between the two black hole spacetime and the pure Brill wave spacetime. This spacetime is especially convenient for the study of black hole dynamics because it is, in a certain sense, a superposition of the Schwarzschild spacetime, which contains a bridge but no radiation, and the pure Brill wave spacetime, which contains radiation but has no bridge (although a black hole may form if the radiation is sufficiently strong). Hence the initial data may be set up to study any number of situations representing the interaction of a time symmetric, axisymmetric cloud of gravitational radiation with a black hole, from the perturbation of a hole by a low intensity wave up to the collision of a hole with a wave whose mass is many times the mass of the hole. The evolution of this data set also may simulate the late stages of the collision of two black holes, as a highly distorted black hole is expected to form as the holes merge. Comparisons of the evolution of these data sets with two black hole data sets will be presented in Refs. [10,11].

The data is computed on an initial hypersurface with the hypercylinder ($\mathbf{S}^2 \times \mathbf{R}$) topology familiar from the maximally extended Schwarzschild solution. Hence we have two asymptotically flat "sheets" connected through a two-sphere, called a throat or bridge. The canonical picture is an isometric embedding into a flat three-space

*Present address: Department of Mathematics, Statistics and Computing Science University of New England, Armidale, NSW 2351, Australia.

of the equatorial plane of the Schwarzschild $t = 0$ slice (see Sec. IV) which has cylindrical topology and is geometrically a parabola of revolution [see Fig. 6(b)].

In the pure Brill wave spacetime the "ground state" (zero Brill wave amplitude) is the Minkowski spacetime while in the black hole plus Brill wave spacetime it is the Schwarzschild spacetime. The scenario is that of a scattering problem: there is some incoming radiation from past null infinity incident on a spherically symmetric *white* hole. The white hole is deformed by the incoming radiation, in the process emitting radiation of its own and losing mass. The two radiation fields combine in such a way to form a surface of time symmetry upon which they are momentarily "at rest." This leaves the field in a state where there is momentarily zero propagation of energy (the "Poynting vector" [Bel-Robinson vector] of the field vanishes): the radiation energy manifests itself by the curvature of the spacetime and by its influence on the shape of the hole. At this moment the hole attains its minimum mass and switches from white to black. The spacetime then duplicates itself: the black hole absorbs radiation, increases in mass, and finally becomes spherical once again.

This paper discusses the properties of the time symmetric slice. A previous paper [9] analyzed the evolution of perturbations from spherical symmetry and future papers will contain results on the evolution of large amplitude initial data (see also [19] and for further properties of the time symmetric slice see [20]). The history of this type of problem in general relativity is as follows. The first numerical construction of a single distorted Einstein-Rosen bridge was by Collins and Williams [12] using the method of Regge calculus; however the problem was only briefly touched upon by them and no detailed analysis of the data was given. The formulation of the initial-value problem we use was used by Brill [13] to give an example of the positivity of mass of a vacuum time symmetric slice. Wheeler [14] contains an extensive physical examination of Brill's initial data set (which we call time symmetric Brill waves). Both Eppley [6,7] and Miyama [8] have numerically computed the initial data and evolution of the Brill wave spacetimes. Abrahams [15] and Abrahams and Evans [16] also compute vacuum pure wave solutions which are similar, though not identical in form, to the pure Brill wave spacetimes.

This paper is organized as follows. Section II describes the form of the initial three-metric and extrinsic curvature. Section III discusses the mass of the initial hypersurface. Section IV discusses various aspects of the geometry of the initial slice mostly through the use of embedding diagrams. Sections V and VI contain an investigation of the location and geometry of apparent horizons on the initial slice. Section VII exhibits the form of various curvature and radiation measures usually examined in numerical relativity calculations, while Sec. VIII gives a linearized analysis of the data. Finally Sec. IX summarizes the work. The Appendix contains an explanation of the numerical methods used in the solution of the initial-value problem and the apparent horizon equation.

We use geometrized units throughout: $G = c = 1$. Greek indices will run from 0 to 3, latin indices from 1 to 3. Four-dimensional quantities will be denoted by a prefixed superscripted (4), e.g., ${}^{(4)}R_{\mu\nu\alpha\beta}$. Three-dimensional quantities will have no prefix.

II. FORM OF INITIAL THREE-METRIC

The initial-value problem of general relativity consists of finding a three-metric γ_{ab} and extrinsic curvature K_{ab} which satisfy the Hamiltonian and momentum constraints:

$$R + (\mathrm{tr}K)^2 - K^{ab}K_{ab} = 0, \tag{1}$$

$$D_b(K^{ab} - \gamma^{ab}\mathrm{tr}K) = 0. \tag{2}$$

Here R is the scalar curvature and D_a the covariant derivative associated with γ_{ab}. As is well known (e.g., [17]) making the initial slice a spacetime isometry surface (i.e., time symmetric) requires the extrinsic curvature tensor to vanish. Such a slice, usually labeled $t = 0$, is called a time symmetric surface because the spacetime in the region $t < 0$ is isometric to the spacetime in the region $t > 0$. Hence on such a surface the momentum constraint is satisfied identically.

This leaves only the Hamiltonian constraint, $R = 0$, to determine the entire three-metric. We follow York and co-workers (e.g., [18]) by writing the three-metric in conformal form

$$\gamma_{ab} = \Psi^4\hat{\gamma}_{ab}. \tag{3}$$

The conformal transformation of the scalar curvature is

$$R = \Psi^{-4}\hat{R} - 8\Psi^{-5}\hat{\Delta}\Psi, \tag{4}$$

and the Hamiltonian constraint becomes the linear equation

$$\hat{\Delta}\Psi = \tfrac{1}{8}\Psi\hat{R}, \tag{5}$$

where quantities with carets are formed out of $\hat{\gamma}_{ab}$ in the usual way.

At this stage one chooses $\hat{\gamma}_{ab}$ and solves Eq. (5) for Ψ. A common choice is to let $\hat{\gamma}_{ab}$ be a flat metric, so that $\hat{R}$ vanishes, in which case the Hamiltonian constraint reduces to the flat space Laplace equation

$$\hat{\Delta}\Psi = 0. \tag{6}$$

For a manifold with a single throat the only asymptotically flat, inversion symmetric solution is the spherically symmetric Schwarzschild solution [19] and so we are forced to find another form for $\hat{\gamma}_{ab}$.

Brill [13] has described a method in which time symmetric initial data takes on a particularly simple form. He originally used the method to prove the positivity of the mass of a vacuum, time symmetric, asymptotically flat hypersurface with $\mathbf{R}^3$ topology. We adapt his method here to calculate axisymmetric initial data for a hypersurface of $\mathbf{S}^2 \times \mathbf{R}$ topology. This is the Einstein-Rosen

bridge topology familiar from the Schwarzschild solution (see [21]). In this work we have followed Misner [22], York and co-workers (e.g., Bowen [23]), and others by requiring the hypersurface to have two isometric regions, usually called "sheets." This creates an inner boundary, called the isometry surface (which on the Schwarzschild $t = 0$ surface coincides with the event horizon), and an isometry operator which maps each sheet onto the other in a metric preserving fashion. We have also chosen the initial data to be equatorial plane symmetric. The calculation therefore takes place on a region bounded by the axis of symmetry ($\theta = 0$), the equator ($\theta = \pi/2$), the isometry surface, and an outer boundary far from the isometry surface.

Choosing spherical polarlike coordinates we let γ_{ab} take the form

$$ds^2 = \Psi^4 \left[e^{2q}(d\rho^2 + \rho^2 d\theta^2) + \rho^2 \sin^2\theta d\phi^2\right]. \tag{7}$$

The conformal metric has scalar curvature

$$\hat{R} = -2e^{-2q}\rho^{-2}\left(\frac{\partial^2 q}{\partial \rho^2} + \frac{\partial^2 q}{\partial \theta^2} + \frac{\partial q}{\partial \rho}\right), \tag{8}$$

and the Hamiltonian constraint becomes

$$\frac{\partial^2\Psi}{\partial\rho^2} + \frac{1}{\rho^2}\frac{\partial^2\Psi}{\partial\theta^2} + \frac{2}{\rho}\frac{\partial\Psi}{\partial\rho} + \frac{1}{\rho^2}\frac{\partial\Psi}{\partial\theta}\cot\theta = -\frac{1}{4}\Psi\left(\frac{\partial^2 q}{\partial\rho^2} + \frac{1}{\rho^2}\frac{\partial^2 q}{\partial\theta^2} + \frac{1}{\rho}\frac{\partial q}{\partial\rho}\right). \tag{9}$$

The function q must satisfy a set of boundary conditions but is otherwise arbitrary. Specifically Brill showed that in order for the mass of the hypersurface to be well defined, q must have the behavior

$$q(\rho, 0) = 0, \quad \lim_{\rho\to\infty} q = O(\rho^{-2}). \tag{10}$$

In this work we have chosen a different radial coordinate, η, related to ρ by $\rho = (m/2)e^{\eta}$, in which the line element takes the form

$$ds^2 = \Psi^4 \left[e^{2q}(d\eta^2 + d\theta^2) + \sin^2\theta d\phi^2\right]. \tag{11}$$

The coordinate η is dimensionless, with m appearing as a length (or mass) scaling parameter (in spherical symmetry we have $m = M$). The Hamiltonian constraint (9) is transformed into

$$\frac{\partial^2\Psi}{\partial\eta^2} + \frac{\partial^2\Psi}{\partial\theta^2} + \frac{\partial\Psi}{\partial\theta}\cot\theta = -\frac{1}{4}\Psi\left(\frac{\partial^2 q}{\partial\eta^2} + \frac{\partial^2 q}{\partial\theta^2} - 1\right). \tag{12}$$

In this work we choose q to be of the form

$$q = af(\theta)g(\eta). \tag{13}$$

The radial dependence is chosen to be the inversion symmetric Gaussian

$$g = e^{-(g_+)^2} + e^{-(g_-)^2}, \tag{14}$$

with

$$g_\pm = \frac{\eta \pm b}{w}. \tag{15}$$

The angular dependence is given by the function f, which in this paper is chosen to be

$$f = \sin^n\theta, \tag{16}$$

where n is an even integer, usually 2 or 4 (unless otherwise stated it will be assumed that $n = 2$). The function q has three independent parameters a, b, and w which specify its overall amplitude and the range and the width of the radial function g. Throughout this work we will refer to an initial data set generated by q parameters a, b, and w by "initial data set (a, b, w)." (In other papers in this series these parameters are given different symbols, e.g., η_0 for b and σ for w. In each particular paper the symbols are chosen to give the least conflict with the rest of the paper.)

Hence the procedure for obtaining a three-metric which has vanishing scalar curvature is to specify the parameters in q and solve (12) for Ψ. The numerical method is described in the Appendix.

III. MASS

It is well known that no local expression for the energy density of the gravitational field can exist in general relativity. However there does exist a well-defined notion of the total energy of an isolated system as measured by a distant observer. One sees this intuitively; it can be measured by observing the relative accelerations of geodesics (freely falling masses) in the laboratory, a direct measurement of the Riemann tensor.

The total mass energy of an isolated source was originally calculated in the Hamiltonian formulation of general relativity by Arnowitt, Deser, and Misner [24]. Specifically they give the expression

$$M = -\oint_\infty (\gamma_{ab,b} - \gamma_{bb,a})\, dS_a. \tag{17}$$

Here the metric is assumed to be in asymptotically Cartesian coordinates and the metric components are to approach those of a flat Cartesian metric no slower than $O(r^{-1})$. The surface integral is to be evaluated at spatial infinity.

Ó Murchadha and York [25] have examined the Arnowitt-Deser-Misner (ADM) energy and momentum formulas in the conformal decomposition formalism. They derive the three-covariant expression

$$E - \hat{E} = -\frac{1}{2\pi}\oint_\infty \nabla_a\Psi dS^a, \tag{18}$$

for the difference between the energy $\hat{E}$ of the conformal metric and the total energy E of the slice. For a conformally flat metric $\hat{E}$ vanishes and we may compute the ADM mass directly from (18). For a nonconformally flat metric $\hat{E}$ will vanish only if $\hat{\gamma}_{ab}$ has no "$1/r$" parts in its expansion at infinity. This is the case in the Brill wave

three-metric if the function q falls off at least as rapidly as $1/r^2$. Our choice for q actually falls off more rapidly than this, its rate is about

$$q \simeq e^{-\eta^2} \simeq e^{-(\ln r)^2} = \frac{1}{r^{\ln r}}. \tag{19}$$

Hence for our initial three-metric we may write

$$E = -\frac{1}{2\pi} \oint_{\infty} \nabla_a \Psi dS^a. \tag{20}$$

In terms of the metric (11) this is

$$M_{\rm ADM} = -\sqrt{\frac{m}{2}} e^{\eta} \int_0^{\pi} \left(\frac{\partial \Psi}{\partial \eta} - \frac{\Psi}{2} \right) \sin\theta \, d\theta. \tag{21}$$

Since this expression is to be computed on some constant η surface the ADM mass computed from (21) is strictly speaking a quasilocal mass measurement. However the mass does converge to a fixed value as one takes larger and larger values of η (see the Appendix for details).

In this section we propose to compute $M_{\rm ADM}$ as a function of the parameters a, b, and w in the function q. The mass will be expressed in terms of the scaling parameter m which sets the length scale of the problem. This is clearly a completely arbitrary number, there being no physically preferred length or time scales in the Einstein equations. Figure 1 shows the mass as a function of a, b, and w in units of m (see the Appendix for an estimate of the numerical error in this figure).

We first notice that the mass is an initially *decreasing* function of a for $a \geq 0$ (Fig. 2). This is rather counterintuitive, as one expects any additional gravitational wave energy to add to the ADM mass. However, in comparing two data sets, say (0, 0, 1), with $M_{\rm ADM} = m$, and (0.1, 0, 1), with $M_{\rm ADM} = 0.952m$, one is really comparing two entirely unrelated hypersurfaces, that is, hypersurfaces which are contained in different spacetimes. Gravitational wave energy has almost certainly been added, but in the process one may have lowered the mass of the hole in such a way that the total mass of the slice was lessened. In other words, by adding the radiation, the mass of the hole may have been made smaller by some incidental geometrical property of the initial data. For $a < 0$ the situation is different. The mass increases monotonically and very rapidly.

The data contains another peculiarity: for a fixed range and amplitude the mass increases as the width w approaches zero and infinity. The latter is expected since a Gaussian with fixed range encompasses more and more proper volume the larger its width becomes, in effect spreading a wave of fixed amplitude over a larger volume. As the width decreases the total mass initially decreases, because of the smaller volume, and then increases, reflecting the increase in energy one expects for a wave packet with predominantly high frequency components. (Note that when w becomes smaller than about 0.5 the errors increase significantly, as discussed in the Appendix and in [19].)

The variation with respect to the range b is less surprising. The mass tends to be larger when the wave is localized on the throat, dropping off at first as b is increased, and then increasing again. The increase near the throat can be explained by the fact that a is not an absolute amplitude; it is dependent on b. This is because the inversion symmetric Gaussian contains two humps which add together when placed close to each other near the throat. The mass increases apparently without bound as b increases again because of the logarithmic nature of the coordinate η. [One might also be tempted to explain the

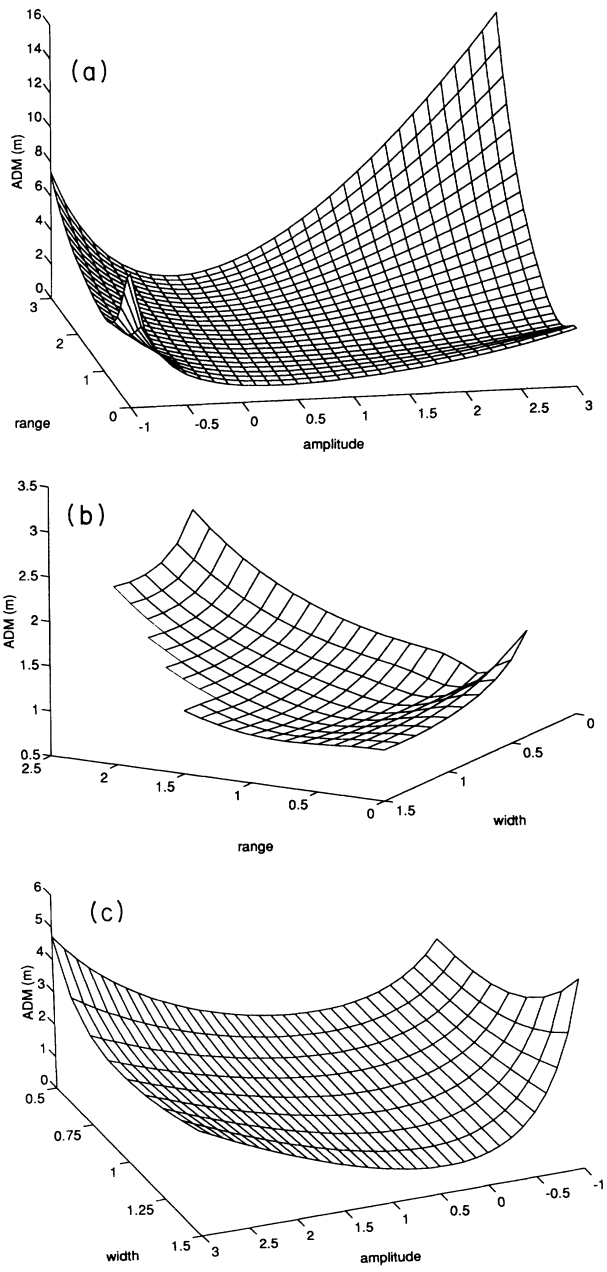

FIG. 1. ADM mass of the initial hypersurface as a function of the Brill wave parameters a, b, and w. (a) The mass as a function of a and b with $w = 1$, (b) as a function of b and w with $a = 1$, and (c) as a function of a and w with $b = 2$. The mass is in units of the scale parameter m. The grid size is 200×53 with the outermost zone at $\eta = 6$.

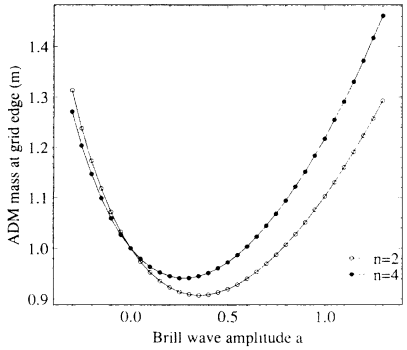

FIG. 2. ADM mass of the initial hypersurface as a function of the Brill wave amplitude a (for range $b = 0$ and width $w = 1$). The mass is in units of the scale parameter m. The grid size is 200×53 with the outermost zone at $\eta = 6$. The hollow (solid) circles denote calculations with the angular parameter $n = 2$ ($n = 4$).

behavior of the mass as a function of b by a (negative) binding energy of the wave to the hole: as b is increased this energy would be responsible for the initial decrease in the ADM mass. This contribution would decrease as b is further increased (presumably like $1/r$) and at some point the increase due to the grid geometry would dominate. However we have not to date found a satisfactory way to formulate this notion (the "interaction energy" defined by Brill and Lindquist [26] does not apply since we have only one Einstein-Rosen bridge)].

In the late 1950s when these types of initial data sets (with $\mathbf{R}^3$ topology) were first being investigated by mathematicians and physicists, it was noted, on physical grounds, that one could not make the amplitude of the Brill wave arbitrarily large. For a too large the slice will not be asymptotically flat; the wave energy will be enough to curve it into closure. Wheeler [14] states the condition elegantly as follows: the mass energy in the wave must not exceed its physical dimensions, roughly, its wavelength. The notion was formalized by Cantor and Brill [27] into the statement that not all asymptotically flat metrics may be conformally related to a physical metric having zero scalar curvature. Specifically they show that if there exists a C^∞ function f with compact support such that

$$\int \hat{R} f^2 d\hat{V} < 8 \int \hat{\gamma}^{ab} \hat{D}_a f \hat{D}_b f d\hat{V}, \tag{22}$$

then $\hat{\gamma}_{ab}$ is not conformally related to a physical three-metric with vanishing scalar curvature. Note that here $\hat{\gamma}_{ab}$ must itself be asymptotically flat. They showed that for Brill waves on $\mathbf{R}^3$ topology slices one may apply (22) and obtain an upper limit on the wave amplitude. Evaluating the condition in the manner of Cantor and Brill, with $f = q$, is inconclusive in the black hole plus Brill wave spacetime because the integration is complicated by the inner boundary on the isometry surface. This boundary leaves a surface integral which is not present in the $\mathbf{R}^3$ case and hence it is possible that there may be both an upper and lower bound on the wave amplitude (it seems likely that there always exists an f which gives an upper bound).

IV. EMBEDDINGS

In this section we will explore the geometry of the three-metric by examining the geometry of various two-dimensional surfaces embedded in the initial slice. This will be done either by computing internal measures of the geometry of the two-surface or by embedding it into a flat three-space.

An embedding diagram is a surface in a fictitious flat three-dimensional space constructed such that it has the same topology and intrinsic geometry as a chosen two-surface in the slice. We have at this point no geometrically or physically distinguished two-surfaces (except for the throat and equator, which are isometry surfaces) and in this situation it is most convenient to begin with the constant coordinate two-surfaces (which include the throat, $\eta = 0$, and equator, $\theta = \pi/2$). In the next section we will consider the apparent horizon and its geometric properties, which is a particular two-surface of physical interest, though not necessarily a constant coordinate surface (in our coordinate system).

There are three choices. The $\eta =$ const surfaces are topologically two-spheres and are surfaces of revolution, the $\theta =$ const surfaces are topologically cylindrical and are also surfaces of revolution, and the $\phi =$ const surfaces are also topologically cylindrical but not surfaces of revolution. Of these surfaces, the first two, because of their symmetry, present no difficulty in embedding (for background see [19]). These embeddings are in fact not uncommon in the general relativity literature (e.g., [3,6,14,22,28,29]). The third has no symmetries whatsoever and embedding surfaces of this (general) type is considerably more difficult. Much is known about the properties of these surfaces but, as a practical matter, the problem of construction has not been definitively solved (see Friedmann [30] for a discussion of the problem).

We begin by examining an embedding of the throat. Figure 3 shows a series of cross sections of the embeddings as a function of the amplitude parameter a. For $a > 0$ the surface is prolate, for $a < 0$ it is oblate, and for a less than about -0.144 no surface exists at all which has the appropriate metric. (The reason is that the Gaussian curvature becomes negative on the axis and this prevents an embedding in a Euclidean space.) The geometry of the throat when $n = 4$ ($f = \sin^4\theta$) is similar to the $n = 2$ case: the embedding is prolate if $a > 0$ and oblate if $a < 0$. Note that for $a > 0$ the embedding takes on a distinct "dumbbell" shape and for $a < 0$ the surfaces are more oblate than the $n = 2$ case. The embedding does not exist if $a < -0.24$.

A similar result has been found previously in a general relativity context by Smarr [28]. He found that the embedding of the event horizon of the Kerr metric becomes more oblate the greater the angular momentum parameter a/M, and it fails to exist at all for $a/M > \sqrt{3}/2$. In

the case of Kerr the oblateness is caused by the angular momentum of the hole, much the same as in a rotating liquid drop. In our case the distortion is caused by the action of the gravitational radiation incident on the hole.

For a given initial data set we may show embeddings of a series of constant η surfaces and obtain an idea of how the distortion changes as η increases. Figure 4 shows such a sequence for the data set $(a, b, w) = (1, 0, 1)$. The surfaces are very prolate near the throat, less so as one moves outward, and by $\eta = 2$ they are nearly spherical. As one might suspect, for data set (-0.144, 0, 1) the surfaces are oblate near the throat and decreasing in oblateness until again by $\eta = 2$ they become spherical. In (1, 1.5, 1) the throat is nearly spherical, the constant η surfaces becoming more and more prolate, reaching a maximum near $\eta = 1.5$, and then becoming spherical again.

Another measure of the geometry of the constant η surfaces which has been used before, e.g., Smarr [28], is the ratio of their polar to equatorial circumference C_p/C_e. As a glance at the embedding diagrams suggests, C_p/C_e is greater than unity for $a > 0$ and less than unity for $a < 0$. In Table I we show the ratio for the throat as a function of a with $b = 0$ and $w = 1$. Note that as the amplitude is increased the distortion can become quite large, with C_p/C_e exceeding 100 for $a > 3$. As in the embedding diagrams it is instructive to see the ratio for a family of constant η surfaces. We show two such families in Figs. 5(a) and 5(b). In Fig. 5(a) the ratio C_p/C_e is shown for the family $(a, 0, 1)$ where the wave is centered on the throat, and in Fig. 5(b) it is shown for the case $(a, 2, 1)$ where the wave is centered away from the throat at $\eta = 2$. Again, for a positive the ratio is greater than unity and for a negative it is less than unity. Note that for a negative the ratio apparently may become very small. This is not possible for surfaces in flat space. Consider a very thin disk in flat space with radius r and thickness d. As d/r becomes very small the polar circumference approaches $4r$, the equatorial circumference $2\pi r$, and the ratio approaches the limiting value $2/\pi$ (≈ 0.637). Thus, for axisymmetric surfaces embedded in a flat space the ratio C_p/C_e cannot be smaller than $2/\pi$. For the throat this value is passed at about $a = -0.34$. That the initial slice permits such a surface is an indication of its deviation from both Euclidean geometry and the spherically symmetric geometry of the Schwarzschild initial slice.

Now let us turn to the constant θ embeddings. Here we have the slight complication that surfaces other than $\theta = \pi/2$ are endowed with a conical "skew." One can see this clearly by imagining the constant θ surfaces of the usual spherical polar coordinates in flat space; they are cones with opening angle θ, except for $\theta = \pi/2$ which is a plane, and $\theta = 0$, which is a line. In general $\theta = 0$ is a one-dimensional curve for which no embedding can be defined (curves have no intrinsic geometry). Hence we explore embeddings of the equator only. (This is the tactic of Wheeler [14], Eppley [6], and Bardeen [29].) Recall that the spherically symmetric embedding is the parabola of revolution [Fig. 6(b)], in cylindrical coordinates

$$z = \sqrt{8M(r - 2M)} \tag{23}$$

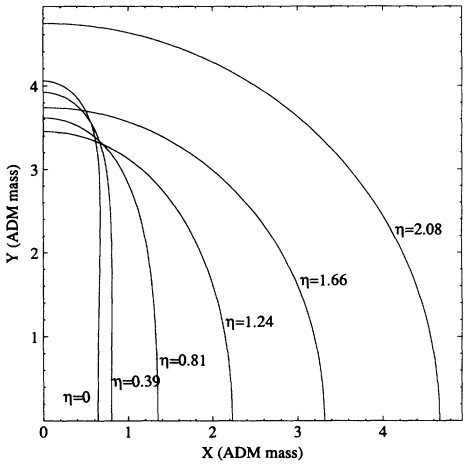

FIG. 4. Embedding of a series of η = const surfaces for the initial data set $(a, b, w) = (1, 0, 1)$. The flat space axes are in units of $M_{\rm ADM}$. The grid size is 200 × 53 with the outermost zone at $\eta = 6$. As one moves away from the throat the surfaces are less prolate, becoming spherical at large radius.

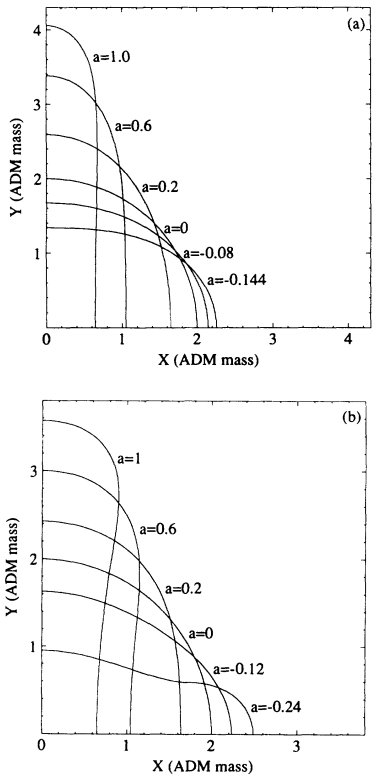

FIG. 3. (a) Embedding of the throat ($\eta = 0$) into a flat three-space as a function of the amplitude a with range $b = 0$, width $w = 1$ and angular parameter $n = 2$. The flat space coordinates are in units of the ADM mass for each data set. The grid size is 200 × 53 with outermost zone at $\eta = 6$ in each case. Positive values of the amplitude produce prolate geometries while negative values produce oblate geometries. (b) The same embeddings with angular parameter $n = 4$.

TABLE I. Ratio of polar to equatorial circumference of the surface $\eta = 0$ as a function of the amplitude a with $b = 0$ and $w = 1$. The grid size is 200×53 with the outermost zone at $\eta = 6$.

a	-1.0	-0.5	0.0	0.5	1.0	1.5	2.0	2.5	3.0
C_p/C_e	0.2803	0.5189	1.000	2.020	4.282	9.497	21.90	52.14	127.2

or, in parametric form,

$$z = 4M \sinh(\eta/2), \quad r = 2M \cosh^2(\eta/2). \tag{24}$$

A few samples of equatorial embeddings for different distortion parameters are shown in Fig. 6. For $a > 0$ the embeddings retain the basic shape of the spherically symmetric case, but for larger amplitudes the throat becomes longer and thinner. For $a < 0$ the diagrams show the formation of a shape reminiscent of the classic "bag of gold" geometry [14]. Wheeler [14] and Eppley [6] both found

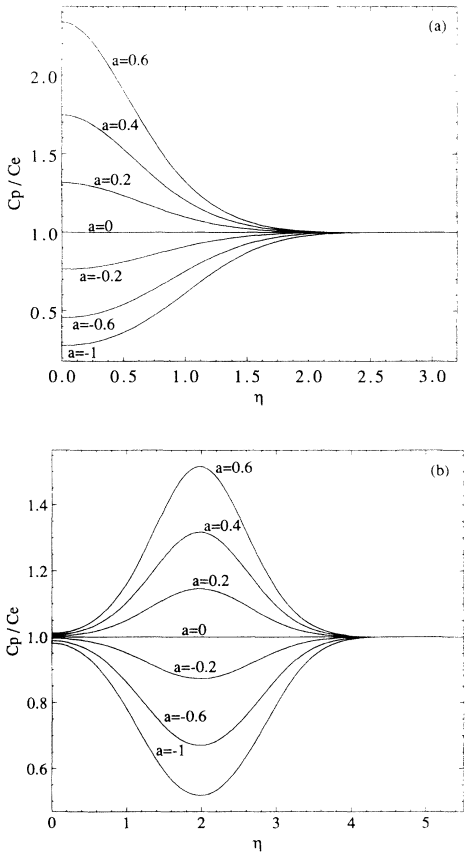

FIG. 5. (a) The ratio of the polar to equatorial circumferences, C_p/C_e, of the constant η surfaces as a function of η and the Brill wave amplitude a is shown for family of spacetimes $(a, b, w) = (a, 0, 1)$. The grid size is 200×53 with the outermost zone at $\eta = 6$. As before, negative amplitudes lead to oblate surfaces and positive amplitudes produce prolate surfaces, and the surfaces become spherical away from the throat. (b) C_p/C_e is shown for the family $(a, b, w) = (a, 2, 1)$. The same trend for positive (negative) amplitudes to produce prolate (oblate) surfaces is seen, but the maximum distortion is found where the wave is centered, the surfaces becoming spherical both near and far from the throat.

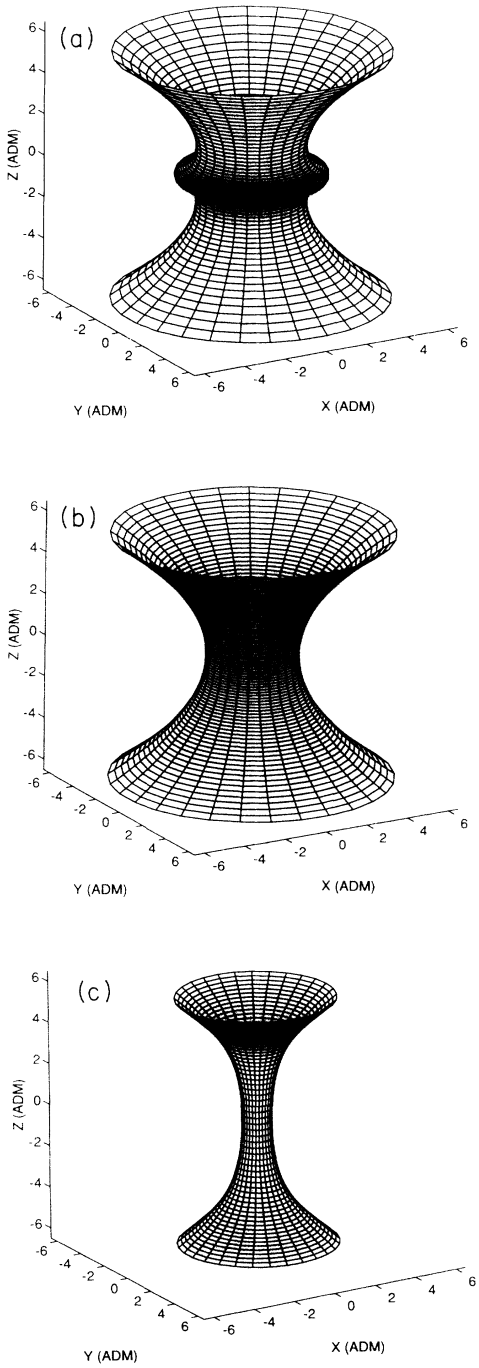

FIG. 6. Isometric embeddings of the equatorial plane for initial data sets $(a, 0, 1)$ with $a = -0.59$ (a), $a = 0$ (b), and $a = 1$ (c). The diagrams are each plotted out to proper distance $8M_{\rm ADM}$ (about $\eta = 2.7$ in each case) and the flat space coordinates are in units of the respective ADM masses. As the amplitude a becomes more negative, the geometry develops a shape akin to the classic "bag of gold."

this type of geometry for the embedding of the equator for "pure" Brill waves, that is, Brill waves on a Euclidean topology. For this topology a bag of gold occurs when a minimal area surface appears. The existence and location of minimal area surfaces is an important physical problem and is taken up in the next section. In our case, as we shall see, the throat is automatically an extremal area surface and therefore a bag of gold will be produced if a minimal surface occurs outside of the throat. Note that since we are looking at the equator only it remains unclear that, for example, $(-0.59, 0, 1)$ really represents a bag of gold. We shall see in the next section that in fact $(-0.59, 0, 1)$ has no extremal area surfaces other than the throat; the throat is a global minimum.

We note that for $a < -0.59$ the diagrams do not exist. The reason for this is that, as seen in Fig. 6(b), they are beginning to "fold over," i.e., become horizontal, just outside of the throat. It turns out to be rather difficult for a surface of revolution to perform this particular geometrical feat (this is explained in more detail in [19]) and so this result is not particularly surprising.

Again the equatorial embeddings for the $n = 4$ data sets are similar to the $n = 2$ data sets. The embeddings "fold over" and cease to exist at $a = -0.59$ in this case as well.

V. APPARENT HORIZONS

A compact orientable two-surface is said to be trapped if its outgoing normal null congruence has negative divergence over the entire surface and marginally trapped if the divergence is exactly zero over the surface. On an asymptotically flat hypersurface the outermost marginally trapped surface is called the apparent horizon. Trapped surfaces are generally spacelike or null and since matter or radiation may cross a spacelike or null surface from one side only they behave as one-way membranes, in much the same way as event horizons [31]. In a celebrated theorem, Penrose [32] showed that the formation of a trapped surface in a spacetime signals the onset of a spacetime singularity and it can be shown that if a trapped surface exists in a spacetime then it necessarily lies within an event horizon, assuming the cosmic censorship hypothesis holds. (For information about the apparent and event horizons during the evolution of these initial data sets see [10,19,33].)

If k^μ is the outward pointing null normal to a two-surface $\mathcal{S}$ then the condition that $\mathcal{S}$ be a marginally trapped surface is that the divergence of k^μ vanish:

$$\nabla_\mu k^\mu = 0. \tag{25}$$

This may be translated [18,34] into a condition on the unit spatial normal s^a of $\mathcal{S}$

$$\nabla_\mu k^\mu = D_a s^a - \mathrm{tr}K + K_{ab} s^a s^b = 0. \tag{26}$$

On a time symmetric slice this reduces to the "minimal surface" condition

$$D_a s^a = 0 \tag{27}$$

and the properties of apparent horizons are particularly amenable to analysis.

Gibbons [35] has shown that an isometry surface is also one of extremal area; this means that the throat of our initial slice is automatically a marginally trapped surface. In addition he shows that any minimal area surfaces occurring on a slice with non-negative scalar curvature must be of spherical topology. On a time symmetric slice the scalar curvature vanishes by the Hamiltonian constraint and so all minimal area surfaces are of spherical topology. Note that the apparent horizon, being the outermost trapped surface, must be minimal in area. Hence the apparent horizon on a time symmetric hypersurface must be a two-sphere. (Hawking [36] shows that the apparent horizon must have spherical topology at all times.)

Now the aim of this section is to find and examine apparent horizons on the initial hypersurface. Given the above we are already well on our way: we know that there always exists at least one trapped surface, the throat, which by construction of the manifold is always of spherical topology. If a minimal surface should occur outside the throat we know that it too must be a two-sphere. Given an initial data set the usual strategy, and the one adopted here, is to attempt to find two-surfaces satisfying Eq. (27) by an iterative procedure. We use the method of Cook [34] which converges on solutions given a sufficiently good initial guess. The relevant equations, numerical properties of the method, and accuracy of the solutions are described in the Appendix. Here we state that in general searches for apparent horizons were done systematically, using a variety of initial guesses, and that reasonable care was taken to assure that the solution found was indeed the outermost trapped surface.

We first discuss the location of the apparent horizon. We know that in spherical symmetry the apparent horizon is located at $\eta = 0$. Given the equatorial embedding diagram [Fig. 6(b)] of the previous section we may suspect that a new minimal surface will form for a sufficiently less than zero. On the other hand it appears the for $a > 0$ no new minimal surfaces will form. In fact, a minimal surface outside of the throat will form in both cases as long as $|a|$ is sufficiently greater than zero. With the wave centered on the throat ($b = 0$) and $w = 1$ new extremal area surfaces are found if $a > 3.03$ or $a < -0.65$; for $-0.65 < a < 3.03$ the throat remains the apparent horizon. Figure 7 shows the coordinate position $\eta(\theta)$ of the apparent horizon. In most cases the horizons are found to be quite close to the $\eta = \text{const}$ two-spheres (this holds for the $n = 4$ cases as well). Note that an outer minimal surface does not form *until* $a \leq -0.65$. Hence the embeddings in Fig. 6 have no minimal surfaces other than the throat. This result is more or less in consonance with Eppley's [6] and Miyama's [8] results on apparent horizons in Brill wave spacetimes. However Eppley found that the new apparent horizon occurs more or less simultaneously with the suggestive bulge in the equatorial embedding diagrams; here the bulge is seen at a significantly lower amplitude than where the new apparent horizon occurs. It should be remarked that they worked on a manifold with Euclidean topology and used a quantitatively different q function, one which fell off as

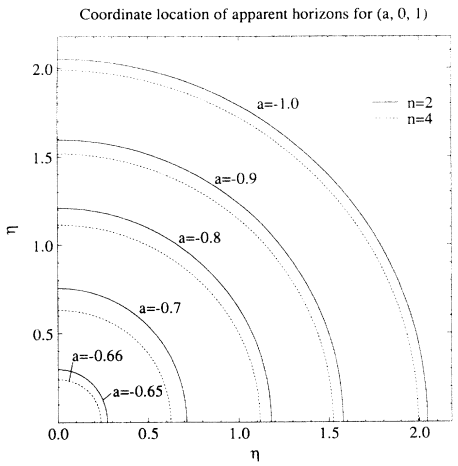

FIG. 7. Apparent horizons on the initial hypersurface for the data sets determined by $-1.0 \leq a \leq -0.65$, $b = 0$, and $w = 1$. The left vertical axis represents the symmetry axis ($\theta = 0$) and the lower horizontal axis is the equator ($\theta = \pi/2$). For the amplitude $a > -0.65$ the horizons are all found on the throat ($\eta = 0$). Note that even though the horizons are located near coordinate two-spheres, the intrinsic geometry can be quite distorted. The grid is 200×53 with the outermost zone at $\eta = 6$.

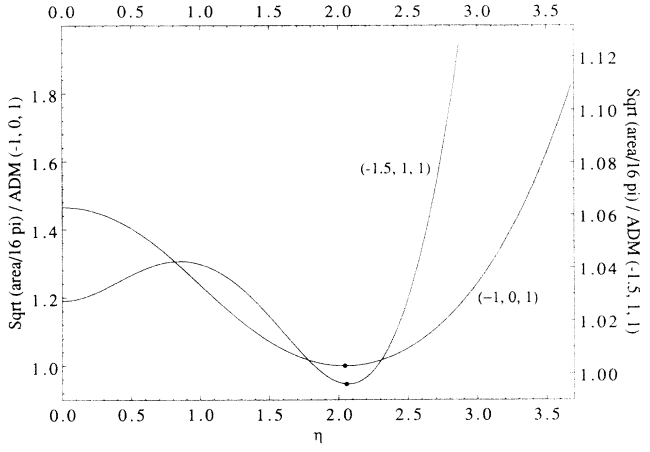

FIG. 8. The area function $(A/16\pi)^{1/2}$ of the constant η two-spheres as a function of η for the initial data sets $(a, b, w) = (-1, 0, 1)$ and $(-1.5, 1, 1)$. The quantity is in units of M_{ADM}. The small dot shows the location of the intersection of the apparent horizon with the equator ($\theta = \pi/2$). The grid is 200×53 with outermost grid point at $\eta = 6$.

r^{-3} rather than $r^{-\ln r}$.

Compressing the Brill wave forces the new minimal surface to appear at a smaller amplitude. For $w = 0.5$ a new minimal surface appears at $a = -0.57$ and $a = 1.36$ rather than $a = -0.65$ and $a = 3.03$ in the case $w = 1$ ($b = 0$ in both cases). This makes sense since one expects concentrated regions of curvature to create trapped surfaces more easily than more extended regions. (Although in our case there does not yet exist a standard, physically meaningful, notion of local mass energy; we apply our intuition strictly on the functional form of q. In addition recall that the mass tends to go up if w is made small enough, indicating that these slices have small concentrated regions of mass energy.)

The method used to find stable minimal surfaces was equally able to find unstable minimal surfaces (i.e., surfaces whose mean curvature vanishes but which may be globally deformed to a surface of smaller area) if a sufficiently good initial guess was made. In both these cases ($b = 0$; $w = 1$ and $w = 0.5$) the throat becomes an unstable minimal surface when the outer trapped surface forms. The area of the η = const two-spheres, plotted in Fig. 8 for the $w = 1$ case, decrease as one moves out from the throat reaching a minimum in the neighborhood of the apparent horizon and then increase without limit. Since the horizon is nearly a coordinate two-sphere we expect the minimum area coordinate sphere to be very near the apparent horizon.

Moving the Brill wave outward should decrease the likelihood of forming a new minimal surface and this is in fact what happens. With $b = 0.5$ a new outer minimal surface appears at $a = -0.84$ and with $b = 1$ this occurs at $a = -1.42$. In the $b = 1$ case there are actually *two* minimal surfaces, the throat and the apparent horizon, with an unstable minimal surface in between them. The area of the constant η surfaces are shown in Fig. 8 for the data set $(-1.5, 1, 1)$. Note that in the $b = 0$ case the apparent horizon appears to disengage smoothly from the throat as a is lowered through -0.65. That is, one can always find an apparent horizon arbitrarily close to the throat for a close enough to -0.65. For the $b = 1$ data sets this is not the case. The horizon appears at $a = -1.42$ in the neighborhood of $\eta = 1.23$. For $a > -1.42$ the horizon stays on the throat; we could not locate any intermediate positions.

The geometry of the apparent horizon, when it coincides with the throat, was discussed in the previous section. For the remainder of this section we will discuss the geometry of these new "outer" apparent horizons. A few things may be guessed from what we already know: the horizons will in general have the geometry of oblate (prolate) spheroids when $a < 0$ ($a > 0$), since this is the case for the constant η surfaces, their ratio of polar to equatorial circumference will be less than (greater than) one, and in general we cannot expect an embedding diagram to exist in every case.

In Fig. 9 we show the polar to equatorial circumference ratio and embedding diagrams for the apparent horizons when the wave is centered on the throat. Note that the apparent horizons become *more* spherical as a is decreased rather than more distorted as in the case when a is near zero. This is because the horizon is moving farther away from the throat where the distortion is concentrated (in these data sets). For these horizons the embedding diagrams do not exist unless a is *less* than about -0.82. The story is much the same for the $b = 1$ cases. The unstable minimal surfaces for these initial data sets are also oblate as are their throats. A typical case is $(-1.5, 1, 1)$ which has C_p/C_e equal to 0.73, 0.38, 0.50 for the apparent horizon, unstable minimal surface, and throat, respectively.

As in the case of the embedding diagrams, the apparent horizons for the $n = 4$ data sets are similar to the data sets with $n = 2$. For a given amplitude the apparent horizons are located at about the same coordinate radius and have similar geometry. Typical cases are the data sets $(a, 0, 1)$. Minimal surfaces appear outside the throat for $a < -0.66$ and $a > 2.4$ which are oblate and prolate, respectively. Data sets $(a, 2, 1)$ have outer minimal surfaces if $a < -2$. In general at high amplitudes $(|a| > 1)$ the $n = 4$ data sets are more likely to form outer an outer minimal surface than the data sets with $n = 2$ for a given set of Brill wave parameters.

VI. RADIATION EFFICIENCY

The second law of black hole dynamics states that the area of the event horizon cannot decrease with time. The law is usually applied in the following manner: Consider a multiple black hole spacetime (i.e., a spacetime which contains a spacelike slice on which the event horizon consists of multiple disjoint surfaces) at a time in which the holes are in a quasistatic state, that is, they are very far apart and have small relative velocities. Add up the "Schwarzschild" masses of the individual holes to obtain a total mass. Look again at the spacetime after some or all of the holes have merged and the system is once again in a quasistatic state. Again add all the "Schwarzschild" masses. The difference between it and the first sum is the maximum possible amount of energy which has been generated (i.e., has escaped to infinity) in the form of gravitational radiation by the coalescence. The fraction of the ADM mass represented by this radiation is usually called the maximum radiation efficiency of the source.

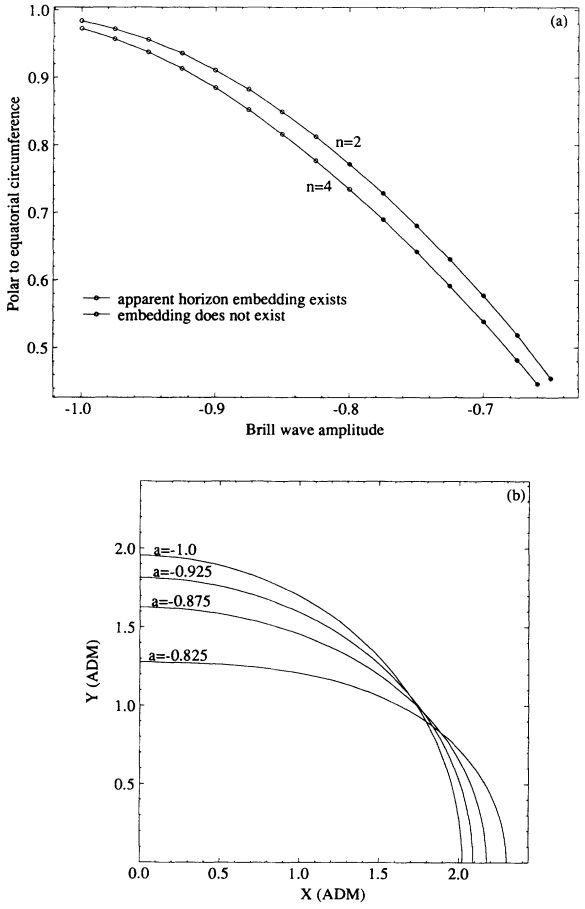

FIG. 9. (a) The ratio of polar to equatorial circumferences of the apparent horizon is shown for various configurations with negative amplitude. All such configurations are oblate. Larger magnitude Brill waves tend to produce *more* spherical geometries. (b) Embedding diagrams for the apparent horizons of initial data sets $(a, 0, 1)$ with $-1 < a < -0.65$ are shown for angular parameter $n = 2$. The flat space coordinates are in units of the ADM mass of each initial data set. The grid is 200×53 with the outermost zone at $\eta = 6$ in each case.

In this section we aim to compute the radiation efficiency of our spacetimes. There are two problems: at this point we have not computed an evolution of the data, and as a consequence we have not located the event horizon, and the data sets do not in general describe quasistatic systems. We proceed as follows: In accord with the second law the *irreducible mass* of a black hole is defined to be [34,37]

$$M_{\rm EH} \equiv \sqrt{\frac{\text{area of event horizon}}{16\pi}}. \tag{28}$$

In analogy to this we define the mass of the apparent horizon to be

$$M_{\rm AH} \equiv \sqrt{\frac{\text{area of apparent horizon}}{16\pi}}. \tag{29}$$

Now on a time symmetric surface the apparent horizon is the outermost minimal area surface hence the only case where the event horizon could have smaller area is if it lay inside the apparent horizon near another local minimal surface. However it can be shown that if an event horizon exists it must lie outside of the apparent horizon [36]. Since (in our case) the apparent horizon is the outermost minimal area surface, any surface lying outside it must have greater area. Thus if there exists an event horizon on the initial slice its irreducible mass must be greater than $M_{\rm AH}$.

The radiation efficiency of an initial data set is defined to be the difference between the ADM mass and the irreducible mass in the final state, long after the hole has become spherical:

$$\text{efficiency} = \frac{M_{\rm ADM} - \text{final } M_{\rm EH}}{M_{\rm ADM}} \leq \frac{M_{\rm ADM} - \text{initial } M_{\rm EH}}{M_{\rm ADM}} \tag{30}$$

$$\leq \frac{M_{\rm ADM} - \text{initial } M_{\rm AH}}{M_{\rm ADM}}. \tag{31}$$

Hence the third fraction in (31) serves as an upper bound on the radiation efficiency of an initial data set. That is, we must have

$$0 \leq \frac{M_{\rm ADM} - \text{final } M_{\rm EH}}{M_{\rm ADM}} \leq \frac{M_{\rm ADM} - \text{initial } M_{\rm AH}}{M_{\rm ADM}} \leq 1. \quad (32)$$

We will call the second fraction in (32) the *maximum radiation loss* (MRL) of an initial data set.

As is well known, the above argument implicitly assumes the cosmic censorship hypothesis. That is, we have assumed that the curvature singularity to the future of $t = 0$ (which we suppose exists) is hidden from future null infinity. Penrose [38] has pointed out that if one could create an initial data set which violates

$$M_{\rm AH} \leq M_{\rm ADM} \quad (33)$$

then the cosmic censorship hypothesis would be in serious jeopardy. Jang and Wald [39] have shown, subject to a certain mathematical condition, that time symmetric hypersurfaces for which the apparent horizon consists of a single component cannot violate Eq. (33). And indeed in the black hole plus Brill wave spacetime we have not found an initial data set in which (33) has not held.

We perform several experiments. In Figs. 10(a) and 10(b) the MRL is shown as a function of the Brill wave parameter a for a wave centered on the throat with unit width w. Figure 10(a) shows results for negative amplitudes, while Fig. 10(b) shows positive amplitude configurations. For $a < 0$ it is an initially increasing function, reaching a maximum of 0.034 at about $a = -0.5$ and then decreasing as a further decreases. As shown in the previous section, an outer minimal surface appears in these data sets for $a < -0.65$. Figure 10(a) shows that the outer minimal surface appears just before the Penrose inequality (33) is violated. Afterward the area of the throat continues to decrease while the area of the outer minimal surface increases so as to just satisfy the inequality. Figure 10(b) shows that for $a > 0$ the MRL is again an increasing function of a. It reaches a maximum of just over 0.3 near $a = 2$ and then decreases, and again, an outer minimal surface forms at $a = 3.03$ before Eq. (33) is violated. The data sets with angular parameter $n = 4$ have similar characteristics. Outer minimal surfaces appear for $a > 2.4$ and $a < -0.66$ in a way which satisfies the Penrose inequality. The cases $a < 0$ with $b = 0.5$ and $b = 1$ are similar to the $b = 0$ case with the exception that the MRL is larger, about 0.05 (at $a = -0.7$) for $b = 0.5$ and about 0.14 (at $a = -1$) for $b = 1$.

Moving the range outward increases the MRL dramatically. In Fig. 11 we show the MRL as a function of a with $b = 2$. Note that in this case it appears as if the curve is turning over as a gets much less than zero, indicating that an apparent horizon would form for those data sets. From this figure we see that it is possible to create initial data sets in which potentially large amounts of radiation may escape to null infinity. Data set (2.8, 2, 1) has $M_{\rm ADM}/M_{\rm AH}$ about 9.4 (MRL = 0.89), while, increasing the range parameter to $b = 3$, for (3.3, 3, 1) it is just over 34 (MRL = 0.97). To emphasize, in this latter case the "wave" part of the initial data contains 97% of the mass of the system, over 30 times the initial mass of the hole.

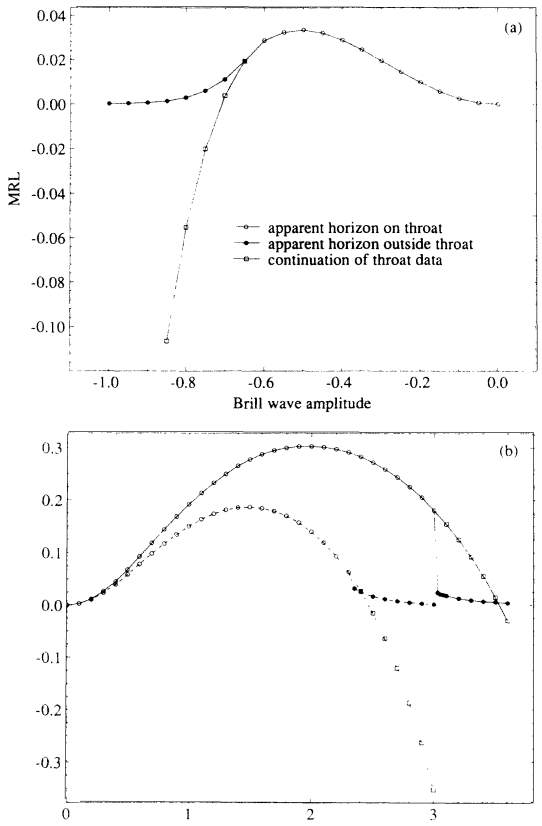

FIG. 10. (a) The maximum radiation loss MRL $= 1 - M_{\rm AH}/M_{\rm ADM}$ as a function of the amplitude a with range $b = 0$, and width $w = 1$, and angular parameter $n = 2$ for amplitudes $a < 0$. Circles are used to mark the data for the apparent horizon, while boxes are used for the throat if the horizon has detached. For $-0.65 < a < 3.03$ the throat is the apparent horizon while for a outside that range the apparent horizon lies outside of $\eta = 0$. The grid size is 200×53 with the outermost zone at $\eta = 6$. (b) The continuation of (a) with $a > 0$. In this diagram we include configurations for both angular parameters $n = 2$ (solid line) and $n = 4$ (dashed line) showing that the apparent horizon detaches from the throat at lower values of the amplitude for the $n = 4$ data sets.

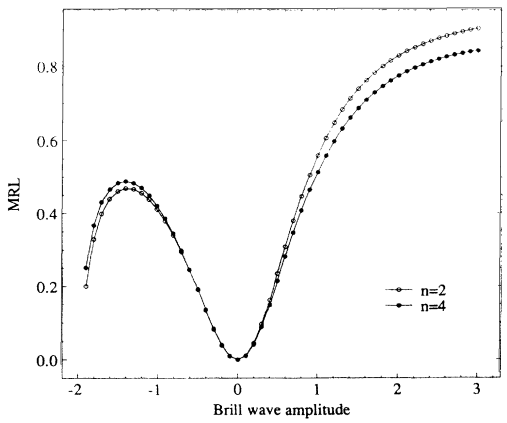

FIG. 11. The maximum radiation loss (MRL) as a function of the amplitude a, with $b = 2$ and $w = 1$ ($n = 2$). The grid size is 200×53 with the outermost zone at $\eta = 6$.

VII. CURVATURE QUANTITIES AND RADIATIVE VARIABLES

In this section we investigate the form of various curvature quantities and radiative variables traditional to numerical relativity calculations. We follow the work of Smarr on the two black hole collision [4], Eppley and Miyama on the pure Brill wave spacetime [7,8], Anninos [40] on plane symmetric cosmologies, and additional work on the evolution of the black hole plus Brill wave spacetime by Bernstein [19]. We will examine the well-known Newman-Penrose spin coefficients and projections of the Weyl tensor, the quadratic curvature invariant I, and the York curvature tensor described in [41]. The often used Bel-Robinson vector vanishes on a time symmetric slice and so cannot be included.

We begin with the curvature invariants of the Riemann tensor. In a general spacetime (one containing matter) 14 independent scalar quantities can be formed out of the Riemann tensor [42–44,18,45]. In a spacetime containing only electromagnetic fields the number reduces to nine, and in a vacuum spacetime there are only four. The simplest of these is the "square" of the Riemann tensor, usually denoted I,

$$2I = {}^{(4)}R^{\mu\nu\alpha\beta}\,{}^{(4)}R_{\mu\nu\alpha\beta} \tag{34}$$

and on a time symmetric slice this reduces to the simple form

$$I = 4R^{ab}R_{ab}. \tag{35}$$

For the Schwarzschild solution it is a straightforward affair to compute

$$I = \frac{24M^2}{r^6} = \frac{3}{8M^4\cosh^{12}(\eta/2)}, \tag{36}$$

where r is the Schwarzschild radial coordinate. Spatial variation of I has been used in the past as a means of tracking the propagation of gravitational radiation [4,8] in the sense that it appears to match well with other measures of the radiation during the evolution (in particular with the Bel-Robinson tensor).

In specific gauges the Newman-Penrose quantities have precise physical interpretations [46]. However in a 3+1 calculation it is usually impractical to compute the quantities in these gauges and here we resort to evaluating the quantities in a convenient, albeit relatively unphysical, manner.

In order to compute the Newman-Penrose quantities we must choose a specific null tetrad. This may be reduced to choosing a family of two-surfaces which foliates the t = const hypersurfaces and for convenience we have chosen the constant η surfaces in this work. Hence the tetrad consists of two null vectors k^μ and l^μ orthogonal to each other and to the η = const surfaces, and two complex "null" vectors m^μ and $\overline{m}^\mu$ which span those surfaces. Assuming unit lapse and zero shift on the initial slice and with the three-metric in the form (7) these are

$$l^\mu = \frac{1}{\sqrt{2}}\left(1, -\frac{1}{\Psi^2 e^q}, 0, 0\right), \tag{37}$$

$$k^\mu = \frac{1}{\sqrt{2}}\left(1, \frac{1}{\Psi^2 e^q}, 0, 0\right), \tag{38}$$

$$m^\mu = \frac{1}{\sqrt{2}}\left(0, 0, \frac{1}{\Psi^2 e^q}, \frac{i}{\Psi^2 \sin\theta}\right), \tag{39}$$

$$\overline{m}^\mu = \frac{1}{\sqrt{2}}\left(0, 0, \frac{1}{\Psi^2 e^q}, \frac{-i}{\Psi^2 \sin\theta}\right). \tag{40}$$

The spin coefficients are

$$\begin{aligned} \kappa &= -k_{\mu;\nu}m^\mu k^\nu, & \nu &= l_{\mu;\nu}\overline{m}^\mu l^\nu, \\ \rho &= -k_{\mu;\nu}m^\mu \overline{m}^\nu, & \mu &= l_{\mu;\nu}\overline{m}^\mu m^\nu, \end{aligned} \tag{41}$$

$$\begin{aligned} \sigma &= -k_{\mu;\nu}m^\mu m^\nu, & \lambda &= l_{\mu;\nu}\overline{m}^\mu \overline{m}^\nu, \\ \tau &= -k_{\mu;\nu}m^\mu l^\nu, & \pi &= l_{\mu;\nu}\overline{m}^\mu k^\nu; \end{aligned}$$

$$\begin{aligned} \epsilon &= \tfrac{1}{2}(m_{\mu;\nu}\overline{m}^\mu k^\nu - k_{\mu;\nu}m^\mu m^\nu), \\ \gamma &= \tfrac{1}{2}(l_{\mu;\nu}k^\mu l^\nu - \overline{m}_{\mu;\nu}m^\mu l^\nu), \\ \beta &= \tfrac{1}{2}(m_{\mu;\nu}\overline{m}^\mu m^\nu - k_{\mu;\nu}m^\mu m^\nu), \\ \alpha &= \tfrac{1}{2}(l_{\mu;\nu}k^\mu \overline{m}^\nu - \overline{m}_{\mu;\nu}m^\mu \overline{m}^\nu), \end{aligned} \tag{42}$$

and using the tetrad above these reduce to

$$\mu = \rho, \quad \sigma = \lambda, \quad \beta = -\alpha, \tag{43}$$

$$\tau = \nu = -\pi = -\kappa, \tag{44}$$

$$\epsilon = \gamma = 0, \tag{45}$$

$$\rho = -\frac{1}{2\sqrt{2}\,e^q\Psi^2}\left(q_{,\eta} + \frac{4\Psi_{,\eta}}{\Psi}\right), \tag{46}$$

$$\kappa = \frac{1}{2\sqrt{2}\,e^q\Psi^2}\left(q_{,\theta} + \frac{2\Psi_{,\theta}}{\Psi}\right), \tag{47}$$

$$\sigma = -\frac{q_{,\eta}}{2\sqrt{2}\,e^q\Psi^2}, \tag{48}$$

$$\alpha = -\frac{1}{2\sqrt{2}\,e^q\Psi^2}\left(\cot\theta + \frac{2\Psi_{,\theta}}{\Psi}\right). \tag{49}$$

The relevant projections of the Weyl tensor are

$$\Psi_0 \equiv C_{\mu\nu\lambda\delta}k^\mu m^\nu k^\lambda m^\delta, \tag{50}$$

$$\Psi_1 \equiv C_{\mu\nu\lambda\delta}k^\mu l^\nu k^\lambda m^\delta, \tag{51}$$

$$\Psi_2 \equiv \tfrac{1}{2}C_{\mu\nu\lambda\delta}k^\mu l^\nu \left(k^\lambda l^\delta - m^\lambda \overline{m}^\delta\right), \tag{52}$$

$$\Psi_3 \equiv C_{\mu\nu\lambda\delta}l^\mu k^\nu l^\lambda \overline{m}^\delta, \tag{53}$$

$$\Psi_4 \equiv C_{\mu\nu\lambda\delta}l^\mu \overline{m}^\nu l^\lambda \overline{m}^\delta, \tag{54}$$

which reduce to

$$\Psi_0 = \Psi_4, \quad \Psi_1 = -\Psi_3, \tag{55}$$

$$\Psi_2 = \frac{1}{e^{2q}\Psi^4}\left[-\frac{q_{,\theta}}{2}\cot\theta + \frac{\Psi_{,\theta}}{\Psi}\cot\theta - \frac{\Psi_{,\theta}q_{,\theta}}{\Psi} + \frac{\Psi_{,\eta}q_{,\eta}}{\Psi} + \frac{\Psi_{,\theta\theta}}{\Psi} - \left(\frac{\Psi_{,\theta}}{\Psi}\right)^2 + 2\left(\frac{\Psi_{,\eta}}{\Psi}\right)^2 - \frac{1}{2}\right], \tag{56}$$

$$\Psi_3 = \frac{1}{e^{2q}\Psi^4}\left(\frac{q_{,\eta}}{2}\cot\theta + \frac{\Psi_{,\eta}q_{,\theta}}{\Psi} + \frac{\Psi_{,\theta}q_{,\eta}}{\Psi} + \frac{3\Psi_{,\eta}\Psi_{,\theta}}{\Psi^2} - \frac{\Psi_{,\eta\theta}}{\Psi}\right), \tag{57}$$

$$\Psi_4 = \frac{1}{e^{2q}\Psi^4}\left(\frac{q_{,\theta}}{2}\cot\theta + \frac{\Psi_{,\theta}}{\Psi}\cot\theta - \frac{q_{,\theta\theta}}{2} + \frac{\Psi_{,\theta}q_{,\theta}}{\Psi} - \frac{q_{,\eta\eta}}{2} - \frac{\Psi_{,\eta}q_{,\eta}}{\Psi} - \frac{\Psi_{,\theta\theta}}{\Psi} + \frac{3\left(\Psi_{,\theta}\right)^2}{\Psi^2}\right). \tag{58}$$

In the Schwarzschild solution these take the values

$$\tau = \nu = \pi = \kappa = \epsilon = \gamma = \sigma = \lambda = 0, \tag{59}$$

$$\rho = -\frac{1}{\sqrt{8}\,M}\frac{\tanh(\eta/2)}{\cosh^2(\eta/2)}, \tag{60}$$

$$\alpha = -\frac{1}{\sqrt{32}\,M}\frac{\cot\theta}{\cosh^2(\eta/2)}, \tag{61}$$

$$\Psi_0 = \Psi_1 = \Psi_3 = \Psi_4 = 0, \tag{62}$$

$$\Psi_2 = -\frac{1}{8M^2\cosh^6(\eta/2)} = -\frac{M}{r^3}. \tag{63}$$

Note that for a time symmetric initial data set I is related to the Weyl tensor components by

$$I = 8\left[(\Psi_4)^2 + 3(\Psi_2)^2 + 4(\Psi_1)^2\right]. \tag{64}$$

Finally, York [41] has proposed a measure of curvature for each three-dimensional hypersurface which retains the symmetry properties of the Weyl tensor and characterizes the conformal three-geometry in a natural way. Specifically he constructs the tensor, which we call the *York curvature tensor*:

$$\tilde{\beta}^{ab} = -\tfrac{1}{2}\gamma^{5/6}\epsilon^{aef}\gamma^{bd}R_{def}. \tag{65}$$

Here ϵ^{abc} is the three-dimensional Levi-Civita tensor and R_{abc} is defined to be

$$R_{abc} = D_cR_{ab} - D_bR_{ac} + \tfrac{1}{4}\left(\gamma_{ac}D_bR - \gamma_{ab}D_cR\right), \tag{66}$$

R_{ab} being the Ricci tensor, and R the scalar curvature formed out of γ_{ab}. $\tilde{\beta}^{ab}$ is constructed to be symmetric, traceless, transverse, and conformally invariant.

The point of the York curvature tensor is that, in a formal sense, it captures the 2 dynamical degrees of freedom of the gravitational field. In spherical symmetry it vanishes identically because in this situation all three-metrics may be written in conformally flat form $\gamma_{ab} = \Psi^4 f_{ab}$. The conformal factor Ψ solely determines the field and Ψ may be regarded as a constrained or not freely specifiable part of the gravitational field [17]. In axisymmetry the tensor has only two nonvanishing components (in an appropriate coordinate system) which are related by the transversality condition. Hence it has just one degree of freedom. This again makes sense because in an axisymmetric spacetime one may always eliminate one of the two polarizations of the field by a coordinate transformation (a rotation of the observer). Our examination of the York curvature tensor is purely experimental as little is known about it apart from what is given in Ref. [41]. The work of Anninos [40] and Bernstein [19] suggests that the York curvature acts in some respects like a radiative quantity, much like the Bel-Robinson vector and the Newman-Penrose quantities.

In axisymmetry $\tilde{\beta}^{ab}$ has two nonzero components, which with our initial three-metric are

$$\tilde{\beta}^{13} = -\tfrac{1}{2}(e^q\sin\theta)^{2/3}(q_{,\theta\theta}\cot\theta + q_{,\eta\eta}\cot\theta - q_{,\theta}\cot^2\theta + \tfrac{1}{2}q_{,\theta\theta\theta} - q_{,\theta}q_{,\theta\theta} - q_{,\eta\eta}q_{,\theta} - q_{,\theta} + \tfrac{1}{2}q_{,\eta\eta\theta}), \tag{67}$$

$$\tilde{\beta}^{23} = -\tfrac{1}{2}(e^q\sin\theta)^{2/3}(q_{,\eta}\cot^2\theta + q_{,\eta}q_{,\theta\theta} - \tfrac{1}{2}q_{,\eta\eta\eta} + q_{,\eta}q_{,\eta\eta} - \tfrac{1}{2}q_{,\eta\theta\theta} + q_{,\eta}). \tag{68}$$

Note that since $\tilde{\beta}^{ab}$ is conformally invariant we may compute it exactly given the form of q. The resulting expression is complicated and we do not write it here.

In Fig. 12 we show some of these quantities as surface plots for the initial data set (0.1, 2, 1). To show the variation along the throat more clearly and to give some indication of the topology we have used a radial offset of one (in the η coordinates), the value one being chosen purely for aesthetic purposes. While all of the functions show oscillations near $\eta = 2$, the peak of the function q,

only Ψ_4 and I have maxima there (here I is plotted as the ratio of the computed value to a "spherically symmetric value" computed by (36) with M the ADM mass and r the areal radius of the constant η shell). These two quantities are second order in the derivatives of the metric while σ and $\tilde{\beta}^{ab}$ are first and third orders, respectively. Also note that I has a (relative) peak on the axis rather than on the equator. When the sign of a is reversed this peak occurs on the equator while the peak in Ψ_4 remains on the equator (Ψ_4 vanishes identically on

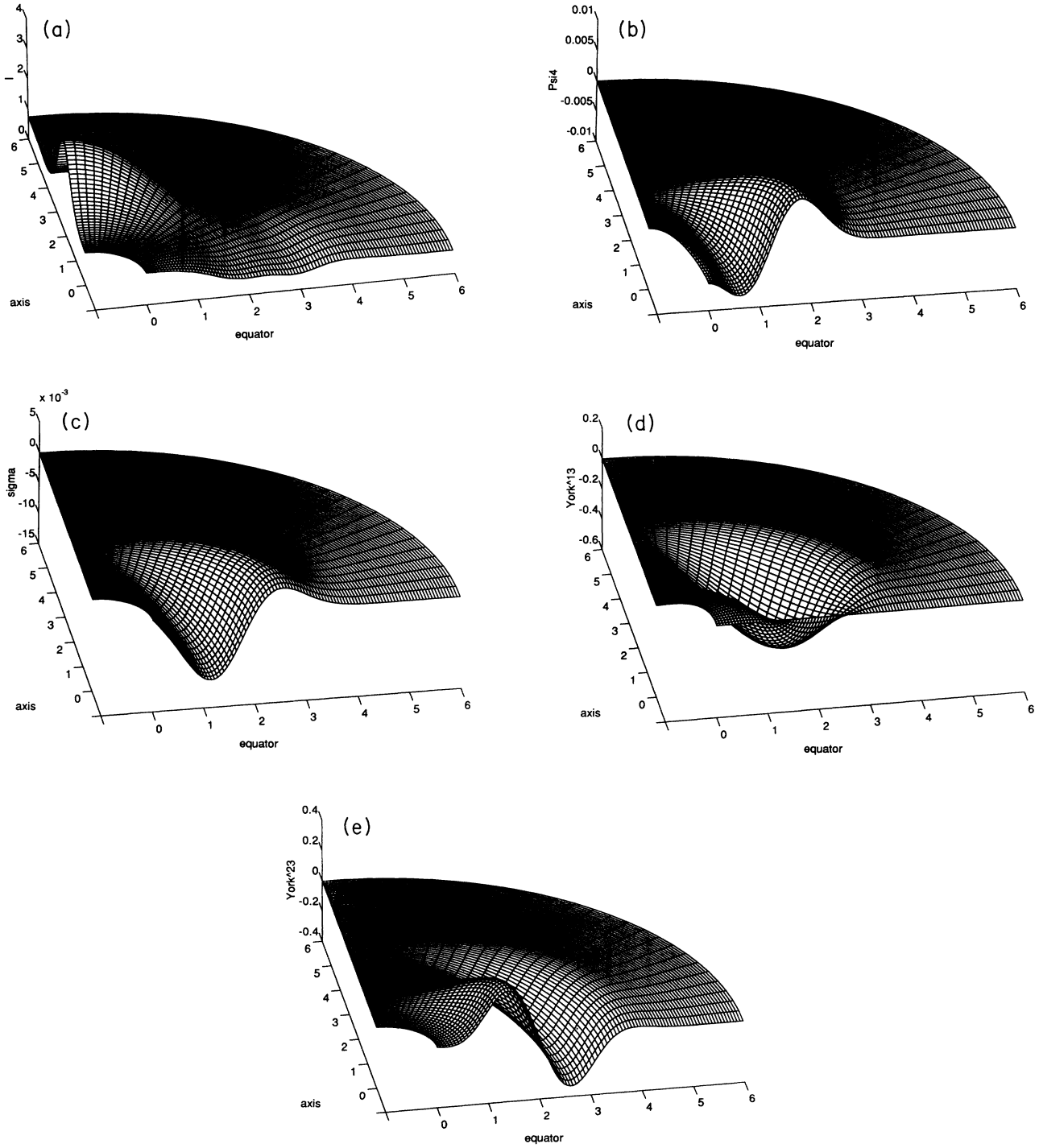

FIG. 12. Various curvature and radiative quantities plotted as a function of η and θ for the data set $a = 0.1$, $b = 2$, $w = 1$. (a) The curvature invariant I divided by the spherically symmetric value (36) using the areal radius of the constant η shell for r and the ADM mass for M. (b) Weyl tensor component Ψ_4, (c) spin coefficient σ, (d) York tensor component $\tilde{\beta}^{13}$, and (e) York tensor component $\tilde{\beta}^{23}$. Each quantity is in the appropriate units of the ADM mass. The grid size is 200×53 with outermost zone at $\eta = 6$ in all cases.

the axis). Figure 13 shows the same plots for I and Ψ_4 when the amplitude is increased to $a = 1$.

VIII. LINEARIZED TREATMENT

In the previous section we have examined a number of radiation indicators based on nonlinear constructions, such as the Weyl tensor. In this section we consider a perturbation expansion of the initial data set about a spherical, Schwarzschild background spacetime. If the Brill wave amplitude a vanishes, the Schwarzschild solution results, so for a small we may appeal to the well-known perturbation theory for black holes to analyze the solution. This analysis is based partly on the wave form extraction technique pioneered by Abrahams [15] that was used in Ref. [9] to obtain wave forms for moderately distorted black holes.

First we consider the spectrum of angular modes (ℓ modes) that are present in the initial data for various choices of the Brill wave function q. If $q = 0$ the solution is spherically symmetric, corresponding to a pure $\ell = 0$ mode. As q is turned on, the black hole becomes distorted in a nonspherical way, inducing higher multipoles in the solution.

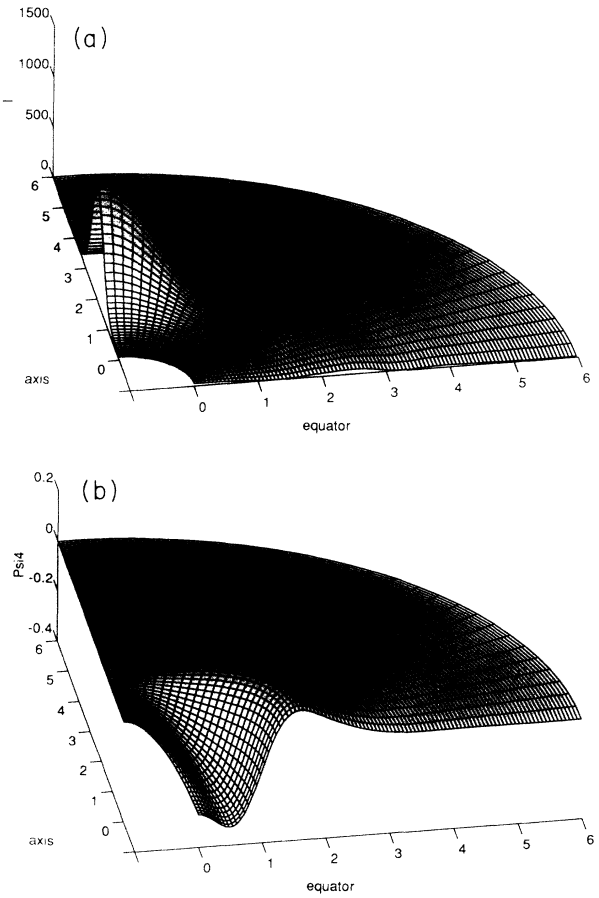

FIG. 13. (a) The curvature invariant I normalized to its spherically symmetric value for data set $a = 1$, $b = 2$, $w = 1$. (b) Weyl tensor component Ψ_4 for the same initial data set. Each quantity is in the appropriate units of the ADM mass. The grid size is 200×53 with outermost zone at $\eta = 6$ in all cases.

The Hamiltonian constraint (12) can be written as

$$\frac{\partial^2 \Psi}{\partial \eta^2} + \nabla_\theta^2 \Psi = -\frac{1}{4}\Psi\left(\frac{\partial^2 q}{\partial \eta^2} + \frac{\partial^2 q}{\partial \theta^2} - 1\right), \tag{69}$$

where ∇_θ^2 is the "theta" part of the laplacian operator. If we expand the functions appearing in this equation in terms of spherical harmonics as

$$\Psi = \sum_{\ell=0}^{\infty} \psi^{(\ell)}(\eta) Y_{\ell 0} \tag{70}$$

and

$$q = \sum_{\ell=2}^{\infty} a q^{(\ell)}(\eta) Y_{\ell 0}, \tag{71}$$

then using the relation

$$\nabla^2{}_\theta Y_{\ell 0} = -\ell(\ell+1) Y_{\ell 0} \tag{72}$$

it is easy to show that for small a the nonlinearity of the Hamiltonian constraint [i.e., the $\Psi q_{,ij}$ terms in (12)] will mix various ℓ modes. For example, if the free function q has the form

$$q = a q(\eta) \sin^2\theta \tag{73}$$

then for small a the resulting solution for Ψ (and hence the metric) will contain $\ell = 2$ terms of linear order in a, but also $\ell = 4$ terms of order a^2. Therefore, even the $n = 2$ data sets will contain an admixture of $\ell = 4$ modes in the initial data, although at second order in the amplitude parameter a. Similarly, the $n = 4$ data sets will contain an admixture of not only $\ell = 2$ (which is present even at linear order in this case because $\sin^4\theta$ itself is a mixture of Y_{20} and Y_{40}), but also $\ell = 6$ at second order in a.

We can extend this analysis to extract the Zerilli function ψ from the initial data. This function is gauge invariant, and its evolution obeys a simple wave equation. It is a direct measure of the gravitational waves present in the system, and was used extensively in the companion paper [9] on the evolution of these black hole data sets. In that paper we examined the time development of the Zerilli function ψ at various fixed coordinate locations. Here we consider the spatial dependence of this quantity in the initial data.

As shown in Ref. [9], the Zerilli function can be extracted by dividing the metric into a spherical background part and a nonspherical perturbation. The perturbation is decomposed in terms of spherical tensor harmonics, and using the orthogonality of these angular functions various ℓ modes of the gauge invariant Zerilli function can be extracted numerically from the initial data. In Fig. 14 we show both the $\ell = 2$ and $\ell = 4$ Zerilli functions for the data set $(a, b, w) = (0.5, 0, 1)$ and angular parameter $n = 2$, with the Weyl tensor compo-

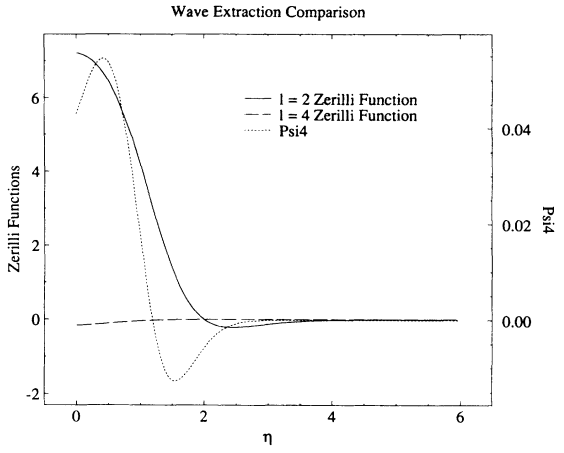

FIG. 14. Three different wavelike quantities are plotted as a function of the radial coordinate η for the initial data set $(a, b, w) = (0.5, 0, 1)$ with angular parameter $n = 2$. The amplitudes of the $\ell = 2$ (solid line) and $\ell = 4$ (long dashed line) extracted Zerilli functions are given by the left vertical scale, while the Weyl tensor projection Ψ_4 (dashed line), measured along the equator $\theta = \pi/2$, is given by the right vertical scale. The nonlinearity of the Hamiltonian constraint generates the $\ell = 4$ contribution to the initial data, as discussed in the text.

nent Ψ_4 along the equator $\theta = \pi/2$ for comparison. As expected, even for $n = 2$ there is a mixture of $\ell = 4$ radiation in the initial data set, although with a much smaller amplitude. (The amplitudes have been normalized as in Ref. [9] to give a true comparison of the energy carried by each ℓ mode, and the quantity Ψ_4 has been normalized as in Ref. [47].) These three different quantities are well correlated spatially, indicating their wavelike nature. Studies of the evolution of such data sets show that for small amplitude, $n = 2$ Brill waves, the $\ell = 4$ mode Zerilli function scales quadratically in the amplitude a, as expected [19].

IX. CONCLUSIONS

We presented a new family of initial data sets for use in studying dynamical axisymmetric spacetimes containing distorted black holes in numerical relativity. These data sets combine the approach of Brill to create a nonlinear vacuum, gravitational wave spacetime, and the Einstein-Rosen bridge construction with an isometry connecting identical three-surfaces across a throat. For simplicity the data sets have been chosen to be time symmetric. We have chosen a particular functional form for the free gravitational wave data in the conformal three-metric, containing four free parameters that specify the shape and amplitude of the free wave data. The Hamiltonian constraint then reduces to a linear elliptic equation for the conformal factor Ψ, which we have solved for a variety of free parameter choices.

If the amplitude of the free data is chosen to vanish, the isometric Schwarzschild solution results. If the amplitude is taken to be small, a slightly distorted Schwarzschild spacetime results that can be analyzed with perturbation theory, and if the amplitude is chosen to be large a highly distorted black hole spacetime is created. Some low amplitude data sets have been evolved and the results have been discussed in Ref. [9]. The evolution of more highly distorted black hole spacetimes are presented in [19].

Of particular interest in black hole spacetimes is their horizon structure. For these initial data sets we have used a method of Cook [48] to find apparent horizons in these distorted black hole systems, and studied their mass and intrinsic geometry. For a certain range of the parameter space of the initial data we find apparent horizons on the black hole throat, or isometry surface. But for other ranges the horizon detaches from the throat and is found outside it. We find that although the *coordinate* shape of the horizon is generally rather spherical, its intrinsic geometry can be extremely nonspherical in this system. Depending on the free wave parameters, the horizon can be oblate or prolate. For the prolate case the horizons can have very long, spindlelike geometries, with the ratio of polar to equatorial circumference exceeding 100:1. If the black hole *event* horizon is strongly distorted, it could raise interesting questions about the hoop conjecture [49–51]. However, whether the event horizons will have similar geometries is a question that can only be answered by evolving these systems. A project to examine the properties of the event horizon for these spacetime is being undertaken and is beginning to yield results [33].

We have also examined the ADM mass of these spacetimes and compared it with the mass of the apparent horizon. In all cases, the ADM mass is found to be greater than the apparent horizon mass, confirming the Penrose inequality (33) for these data sets (see [39]). We have also computed the maximum radiation loss for these spacetimes, defined to be $1 - M_{\rm AH}/M_{\rm ADM}$. For wave data localized near the throat this quantity is generally found to be small (a few percent), but by moving the wave data away from the hole it can be made quite large, approaching 1 in some cases.

A number of other the properties of these initial data sets have been examined, including the Riemann invariant I, the Newman-Penrose projection of the Weyl tensor, and the York curvature tensor. These quantities are often considered as candidates for indicating the presence of gravitational radiation, and have been studied in the dynamical evolution of these data sets [19].

ACKNOWLEDGMENTS

We would like to thank many colleagues with whom we have discussed this work over the last few years, including Greg Cook, Andrew Abrahams, Robert Bartnik, Peter Anninos, John Towns, Roger Ove, and Wai-Mo Suen, among others. This work was supported by NCSA, and calculations were performed on the NCSA Cray Y-MP and the (now decommissioned) Cray 2.

APPENDIX A: THE INITIAL-VALUE PROBLEM

This appendix will discuss the numerical methods used to solve the Hamiltonian constraint (12) and the apparent horizon condition (27). Sections 1 through 3 will discuss the Hamiltonian constraint and Appendix B the apparent horizon finder.

1. Formulation

The initial three-metric is

$$ds^2 = \Psi^4 \left[e^{2q}(d\eta^2 + d\theta^2) + \sin^2\theta d\phi^2\right] \tag{A1}$$

and the equation to be solved for Ψ is the "eigenvalue equation" (12)

$$\frac{\partial^2\Psi}{\partial\eta^2} + \frac{\partial^2\Psi}{\partial\theta^2} + \frac{\partial\Psi}{\partial\theta}\cot\theta = -\frac{1}{4}\Psi\left(\frac{\partial^2 q}{\partial\eta^2} + \frac{\partial^2 q}{\partial\theta^2} - 1\right). \tag{A2}$$

The function q must satisfy a set of boundary conditions but is otherwise arbitrary (though it may not be "too large," see Sec. III).

In addition to axisymmetry we choose the initial slice to be equatorial plane symmetric and isometric through $\eta = 0$. Hence the calculation takes place on a two-dimensional domain with boundaries on the axis of symmetry ($\theta = 0$), the equator ($\theta = \pi/2$), the throat ($\eta = 0$), and an outer boundary (usually $\eta = 6$). Boundary conditions on the three-metric components on the axis and equator can be determined from symmetry conditions. For instance, it can easily be seen that axisymmetry and equatorial plane symmetry require

$$\left.\frac{\partial\gamma_{11}}{\partial\theta}\right|_{\theta=0} = \left.\frac{\partial\gamma_{11}}{\partial\theta}\right|_{\theta=\pi/2} = 0. \tag{A3}$$

To derive the condition on γ_{11} at the throat let the three-metric be written in the spherical polar coordinates (ρ,θ,ϕ) and let the isometry surface be located at radial coordinate $\rho = a$. Let ρ' denote the radial coordinate on the other side of the isometry surface. Then the inversion-through-the-sphere transformation from $\rho > a$ to $\rho < a$ is given by

$$\rho' = \frac{a^2}{\rho}. \tag{A4}$$

By the usual tensor transformation rule we have

$$\gamma'_{11}(\rho' = a) = \gamma_{11}(\rho = a), \tag{A5}$$

where γ'_{11} is the metric component inside $\rho = a$. On the isometry surface this condition, along with continuity of the first derivative gives

$$\left(\frac{\partial\gamma_{11}}{\partial\rho} + \frac{2\gamma_{11}}{a}\right)\Big|_{\rho=a} = 0. \tag{A6}$$

In the (η,θ,ϕ), with $\rho = ae^{\eta}$, coordinates, the inversion transformation (A4) is simply

$$\eta' = -\eta \tag{A7}$$

and the boundary condition (A6) becomes

$$\left.\frac{\partial\gamma_{11}}{\partial\eta}\right|_{\eta=0} = 0. \tag{A8}$$

Now $\gamma_{11} = \Psi^4 e^{2q}$ and so we may evidently choose the boundary conditions for Ψ and q arbitrarily except that together they must satisfy

$$\left(\frac{\partial q}{\partial\eta} + \frac{2}{\Psi}\frac{\partial\Psi}{\partial\eta}\right)\Big|_{\eta=0} = 0. \tag{A9}$$

The first choice, and perhaps the most natural, would be to choose Ψ to have the same conditions as in the Schwarzschild solution where we have $\Psi = \sqrt{2M}\cosh(\eta/2)$. Its boundary conditions are simply

$$\left.\frac{\partial\Psi}{\partial\theta}\right|_{\theta=0} = \left.\frac{\partial\Psi}{\partial\theta}\right|_{\theta=\pi/2} = \left.\frac{\partial\Psi}{\partial\eta}\right|_{\eta=0} = 0. \tag{A10}$$

This choice is the one made throughout this work. Equations (A3) and (A9) give the conditions on q:

$$\left.\frac{\partial q}{\partial\theta}\right|_{\theta=0} = \left.\frac{\partial q}{\partial\theta}\right|_{\theta=\pi/2} = \left.\frac{\partial q}{\partial\eta}\right|_{\eta=0} = 0. \tag{A11}$$

This leaves only an outer boundary condition to determine Ψ uniquely. As York [18] has stressed, the outer boundary condition on Ψ is crucial to obtaining good solutions of the Hamiltonian constraint. In the (ρ,θ,ϕ) coordinates the spherically symmetric solution is

$$\Psi = 1 + \frac{M}{2\rho} \tag{A12}$$

and so one might set $\Psi = 1$ as an outer boundary condition. York has pointed out that this produces an error of order ρ^{-1} at the outer boundary, and he suggests using the Robin condition

$$\frac{\partial\Psi}{\partial\rho} + \frac{\Psi - 1}{\rho} = 0 \tag{A13}$$

which gives an error of order ρ^{-3}. In (η,θ,ϕ) coordinates the spherically symmetric solution of (A2) is $\Psi = \sqrt{2M}\cosh(\eta/2)$ and so there exists no analogue of setting $\Psi = 1$ on the boundary. In this work we have chosen to implement the Robin condition (A13) which in the (η,θ,ϕ) coordinates takes the form

$$\frac{\partial\Psi}{\partial\eta} + \frac{1}{2}\Psi - \sqrt{\frac{m}{2}e^{\eta}} = 0. \tag{A14}$$

The standard procedure for solving Eq. (A2) is as follows: specify a suitable function q, then approximate the Hamiltonian constraint (A2) according to some finite difference scheme and solve the resulting set of coupled

linear equations. Here we have chosen the standard second order centered finite difference operators. Denoting by $\Psi_{i,j}$ the value of Ψ at the grid point labeled by i (the η index) and j (the θ index) we have

$$\frac{\partial \Psi}{\partial \eta} \cong \frac{\Psi_{i+1,j} - \Psi_{i-1,j}}{2\Delta\eta}, \tag{A15}$$

$$\frac{\partial^2 \Psi}{\partial \eta^2} \cong \frac{\Psi_{i+1,j} - 2\Psi_{i,j} + \Psi_{i-1,j}}{(\Delta\eta)^2}, \tag{A16}$$

$$\frac{\partial \Psi}{\partial \theta} \cong \frac{\Psi_{i,j+1} - \Psi_{i,j-1}}{2\Delta\theta}, \tag{A17}$$

$$\frac{\partial^2 \Psi}{\partial \theta^2} \cong \frac{\Psi_{i,j+1} - 2\Psi_{i,j} + \Psi_{i,j-1}}{(\Delta\theta)^2}. \tag{A18}$$

These are substituted into Eq. (A2) resulting in an $n_\eta \times n_\theta$ inhomogeneous linear system for the $n_\eta \times n_\theta$ quantities $\Psi_{i,j}$. [The system is inhomogeneous because of the outer boundary condition (A14).]

The linear system can be solved by a variety of methods. A number of different algorithms were explored and these are discussed more fully in [52]. In this work a generalized conjugate gradient residual method in the package PCGPAK by Scientific Computing Associates was used along with a multigrid code written by Greg Cook and several solvers written by John Towns.

2. Alternative formulations

In spherical symmetry the Hamiltonian constraint (A2) has the solution

$$\Psi(\eta, \theta) = \sqrt{2M}\cosh(\eta/2). \tag{A19}$$

From a purely numerical point of view this is to be contrasted to the solution of the Hamiltonian constraint using the coordinate $\rho = (m/2)e^\eta$:

$$\Psi(\rho, \theta) = 1 + \frac{M}{2\rho}. \tag{A20}$$

The latter form of Ψ has the attractive property of itself asymptotically becoming constant and all its derivatives vanishing. The solution in η coordinates, on the other hand, does not have such behavior. It and all its derivatives are exponentially increasing for large values of η.

The finite difference approximations (A15)–(A18) are derived by expanding the function Ψ in a Taylor series around the point at which the approximations are desired. By manipulating several such series it is possible to get any number of higher order terms to drop out, resulting in an approximation of arbitrarily high order. For instance, the second order approximation of the first derivative comes from making two such expansions and subtracting them. (For the details see [53] Sec. 3.2.) The expression, including truncation error term, reads

$$\frac{\partial \Psi}{\partial \eta} \cong \frac{\Psi_{i+1,j} - \Psi_{i-1,j}}{2\Delta\eta} - \frac{(\Delta\eta)^2}{6}\frac{\partial^3 \Psi}{\partial \eta^3} + O[(\Delta\eta)^4]. \tag{A21}$$

So in the case of an exponentially increasing Ψ the truncation error becomes larger as η increases while in the case of (A20) the ratio of the truncation error to the next leading term decreases as ρ^{-2}. This means that solutions generated in the η coordinates are not going to be as accurate as those generated in (ρ, θ, ϕ) coordinates on the same computational domain.

One solution to the problem is the following: simply factor Ψ in the η coordinates as

$$\Psi = \Psi' \sqrt{\frac{m}{2}}\, e^{\eta/2}, \tag{A22}$$

and solve $R = 0$ for Ψ'. In spherical symmetry the solution is

$$\Psi' = 1 + e^{-\eta}. \tag{A23}$$

Using the transformation $\rho = (m/2)e^\eta$ gives

$$\Psi' = 1 + \frac{m}{2\rho}, \tag{A24}$$

exactly the form (A20) (in spherical symmetry $m = M$). This form of the solution, while having good far zone behavior, suffers from the fact that the isometry inner boundary condition (A9),

$$\frac{\partial \Psi'}{\partial \eta} + \frac{\Psi'}{2} = 0, \tag{A25}$$

is an "anti-Robin" condition: compared to (A13) the Ψ terms have the wrong relative sign since the normal vector to the relevant boundary points in the opposite direction. This condition does not lend itself to the standard proofs of uniqueness for the initial-value problem and can be awkward when used with some standard techniques for solving elliptic equations (see York [18] for comments and references).

Another solution, one which preserves the original boundary condition at the throat, is provided by the factorization

$$\Psi = \Psi' \sqrt{2m}\cosh(\eta/2). \tag{A26}$$

This gives the Hamiltonian constraint the form

$$\frac{\partial^2 \Psi'}{\partial \eta^2} + \frac{\partial^2 \Psi'}{\partial \theta^2} + \tanh(\eta/2)\frac{\partial \Psi'}{\partial \eta} + \frac{\partial \Psi'}{\partial \theta}\cot\theta$$

$$= -\frac{1}{4}\Psi'\left(\frac{\partial^2 q}{\partial \eta^2} + \frac{\partial^2 q}{\partial \theta^2}\right), \tag{A27}$$

and has spherically symmetric solution

$$\Psi' = 1. \tag{A28}$$

The Robin condition takes the form

$$\frac{\partial \Psi'}{\partial \eta} + \Psi' - 1 = 0 \tag{A29}$$

for factorization (A22) and the form

$$\frac{\partial \Psi'}{\partial \eta}(1 + e^{-\eta}) + \Psi' - 1 = 0 \tag{A30}$$

for factorization (A26). Note that m has dropped out of the boundary condition, and hence out of the solution completely. This makes sense since m serves only to set the length scale; i.e., it should "dress" the conformal factor rather than determine it. It stays in the original formulation only because of the outer boundary condition.

Of the three equations, the unfactorized version gave solutions in the widest range of cases. Factorization (A22) was implemented but it generally did not converge in cases where (A26) did, and when it did was no more accurate. The final scheme used to solve the Hamiltonian constraint was to first have the code attempt to solve (A27). If no solution was found then the original unfactorized version (A2) was tried. If no solution was found for this equation as well then the code was stopped.

3. Convergence and accuracy

Once the linear system has been solved we may still ask how well the Hamiltonian constraint (A2) is satisfied. The tolerances on most solvers can be set quite low, so that, for instance, the linear system is satisfied to within a part in 10^{10}. But this is only one measure of how well the Hamiltonian constraint is satisfied and it is a rather artificial one at that. What we have chosen to do is to solve the equation using the centered second order operators and then evaluate the result with the centered fourth order operators (the standard centered fourth order differences were used, e.g., [53]). When this is done the average residual (defined below) is typically much greater than 10^{-10}, in fact, it is usually on the order of $(\Delta\eta)^4 \simeq 10^{-5}$ or so.

The maximum residual of the fourth order system can be used in a convergence test, i.e., the change in the maximum of the residual as finer and finer grids are used indicates whether or not the scheme is convergent and if it is at approximately what rate it is converging. This is fine if one wants to compute convergence rates, since in this case all one needs is the slope of the error as a function of the grid spacing. But for a given grid spacing it would be helpful of one could form a set of quantities upon which a judgment could be made as to the overall accuracy of the solution. In the case of a vacuum spacetime where the constraints must vanish, one cannot *a priori* assign a level to them below which the solution is deemed accurate. That is, with the constraints we have the following question: "How small is small enough?"

One way of gauging this is by the following. In a spacetime with matter the Hamiltonian constraint reads

$$R - K_{ab}K^{ab} + (\mathrm{tr}K)^2 = 2\rho, \tag{A31}$$

where ρ is the mass-energy density of all matter fields (in the frame at rest with respect to observers on the t^μ congruence). In a free evolution scheme where the constraints are not explicitly enforced we generally do not have $\rho = 0$ and one way of measuring the "smallness" of the given left-hand side of (A31) is to compute the total mass it represents and compare that to the known mass of each hypersurface.

We define the residual of the Hamiltonian constraint to be

$$H_{\mathrm{res}} \equiv \frac{8}{\Psi^5 e^{2q}} \left| \frac{\partial^2 \Psi}{\partial \eta^2} + \frac{\partial^2 \Psi}{\partial \theta^2} + \frac{\partial \Psi}{\partial \theta}\cot\theta + \frac{1}{4}\Psi\left(\frac{\partial^2 q}{\partial \eta^2} + \frac{\partial^2 q}{\partial \theta^2} - 1\right)\right|. \tag{A32}$$

And we define the Hamiltonian mass to be the volume integral of the Hamiltonian residual over the computational domain:

$$H_m \equiv \int_V H_{\mathrm{res}} dV = \int_V H_{\mathrm{res}} \Psi^6 e^{2q} \sin\theta d\eta\, d\theta\, d\phi.$$

Here we use the original form of the Hamiltonian constraint (A2) rather than (A27) and retain the overall factor of $8\Psi^{-5}e^{-2q}$ in the scalar curvature. For typical "strong wave" parameters, say (1, 1, 1), H_m/M_{ADM} is about 0.02 while for typical perturbation parameters, say (0.1, 1, 1), it is about 10 times smaller. Also note that if w is much less than 0.5 then the Hamiltonian mass increases sharply. For instance (1, 0, 0.25) has $H_m/M_{\mathrm{ADM}} = 0.37$ (on a 200×53 grid, the standard size for computing almost all the results shown in this paper).

The convergence test is as follows: we pick a set of physical parameters which characterize the initial data in general and plot their values for one particular data set as a function of the number of computational zones. The initial data set chosen is (1, 1, 1). The physical parameters chosen are the ADM mass measured on the outer edge of the grid (M_{ADM}) in units of the scale parameter m, the mass of the apparent horizon M_{AH} in units of M_{ADM}, and from these two the MRL, the ratio of the polar to equatorial circumference of the apparent horizon, the logarithm of the average and maximum of the residual of the Hamiltonian constraint in units of m^{-2}, and the logarithm of H_m in units of M_{ADM}. The apparent horizon is located at $\eta = 0$. The data is shown in Table II, $\log_{10} H_m$ and $\log_{10} H_{\mathrm{max}}$ are plotted in Fig. 15. A least squares linear fit to the data show that the error is decreasing at nearly second order in $\Delta\eta$ and $\Delta\theta$. Note that we have not independently varied the resolution in η and θ as $\Delta\eta$ and $\Delta\theta$ are set to be approximately equal on each grid.

As discussed above, the ADM mass is only properly defined at spatial infinity. Hence although its measurement over a finite two-sphere is converging as the number of grid points is increased, it is converging to some value different than that which would be obtained as a limit when the two-sphere is expanded to infinity. As a consequence the limiting value of M_{ADM} in Table II, unlike the other numbers in the Table (excluding the MRL of course),

TABLE II. Convergence of some of the properties of the initial data set $a = 1$, $b = 1$, $w = 1$. In each case the outermost grid point is located at $\eta = 6$.

	$M_{\rm ADM}$ (m)	$M_{\rm AH}$ ($M_{\rm ADM}$)	MRL	C_p/C_e	$\log_{10} H_m$	$\log_{10} H_{\rm max}$	$\log_{10} H_{\rm average}$
50×14	0.977173	0.699943	0.300057	1.651669	-0.63	-2.88	-3.96
100×27	0.972377	0.701846	0.298154	1.651082	-1.25	-3.47	-4.57
150×40	0.971489	0.702203	0.297797	1.650971	-1.61	-3.82	-4.92
200×53	0.971179	0.702327	0.297673	1.650932	-1.86	-4.07	-5.17
250×66	0.971035	0.702385	0.297615	1.650914	-2.05	-4.26	-5.36
300×79	0.970958	0.702416	0.297584	1.650904	-2.21	-4.42	-5.52
350×92	0.970911	0.702435	0.297565	1.650898	-2.35	-4.56	-5.66
400×105	0.970880	0.702447	0.297553	1.650895	-2.46	-4.67	-5.77

cannot be taken at its face value. In Table III we show the behavior of the ADM mass for spacetime (1, 1, 1) as the outer boundary of the grid is moved outward. The number of grid points and outer boundary value are chosen to make the grid spacing the same for each case. Note that the difference in the ADM mass with the boundary located at $\eta = 6$ (areal radius approximately 209 $M_{\rm ADM}$) and $\eta = 8$ (areal radius approximately 1535 $M_{\rm ADM}$) is only about one part in 10^5.

Finally we point out that the location of the outer boundary is not fixed, but, as a consequence of the fact that the metric of the surface is the solution to the problem, varies according to the input parameters. If a constant η shell has proper area A then we define its areal radius as

$$r_{\rm areal} = \sqrt{\frac{A}{4\pi}}. \tag{A33}$$

In Table IV we show the areal radius of the grid edge in units of m, $M_{\rm ADM}$, and $M_{\rm AH}$ as a function of a with $b = 2$ and $w = 1$. With the outer boundary set at $\eta = 6$ the areal radius of grid edge is $203m$ in spherical symmetry. As the Brill wave amplitude is changed this number remains relatively constant. However since $M_{\rm ADM}$ is varying as a changes the areal radius of the grid edge varies widely if measured in units of $M_{\rm ADM}$. Thus for data set (1, 2, 1) the areal radius of $\eta = 6$ is only about $134M_{\rm ADM}$ and that of (−1, 2, 1) is only about $49M_{\rm ADM}$. Note also that the areal radius of the grid edge can differ by a large factor depending on whether one measures it in terms of the apparent horizon mass or the ADM mass, as in the case of data set (2, 2, 1).

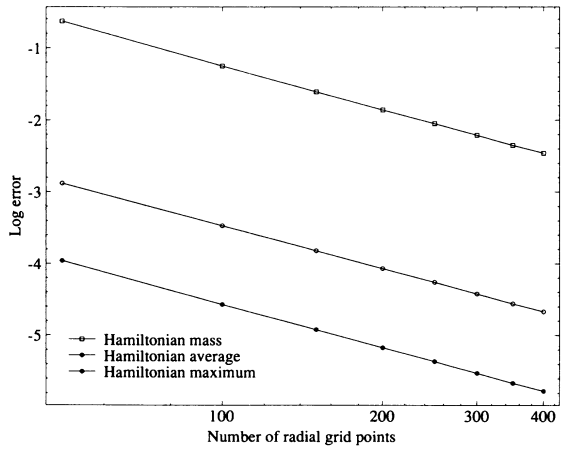

FIG. 15. Convergence of the solution of the Hamiltonian constraint for initial data set (1, 1, 1). The three curves are $\log_{10} H_m$, $\log_{10} H_{\rm max}$, and $\log_{10} H_{\rm average}$ (top, middle, and bottom, respectively). Least squares linear fits to the curves have slopes -2.03, -1.99, and -2.00, respectively. The data is taken from Table II.

APPENDIX B: LOCATION OF APPARENT HORIZONS

This section contains details of the numerical method used to locate the apparent horizons shown in this work. In numerical relativity apparent horizon finding has a long history, primarily associated with two black hole initial data sets. The litany of that research includes Brill and Lindquist [26], Čadež [54], Bishop [55], Nakamura *et al.* [56], and most recently Cook [34]. Important additions were the apparent horizons on the $\mathbf{R}^3$ topology Brill wave initial data sets of Eppley [6] and the horizons on the single Einstein-Rosen bridge manifolds of Cook and York [48]. The research has used a variety of distinctly different methods for locating the horizon. Brill and Lindquist, Eppley, and Nakamura used a numerical method for finding coefficients in a series expansion for the surface. Bishop and Čadež reduced the problem to the solution of an ordinary differential equation which Čadež analyzed as the equations of motion of a particle in a certain potential and which Bishop treated as the geodesic equation for a certain metric. In this work, however, we will use the method of Cook. Like Bishop and Čadež, he treats the problem as finding the solution of a particular ordinary differential equation (ODE), but unlike them he solves the resulting two-point boundary-value problem using a relaxation technique rather than the shooting method. (The recent method of Tod [57] should also be mentioned. He considers the problem as finding the equilibrium state of a parabolic system.)

Given a hypersurface Σ with three-metric γ_{ab} and extrinsic curvature K_{ab} the problem in general is to find the outermost compact, orientable, two-surface $\mathcal{S}$ whose outward pointing spatial unit normal s^a (that is, lying in Σ) satisfies

TABLE III. Value of the ADM mass measured on the outer boundary as a function of the boundary position for initial data set (1, 1, 1). The grid spacing is $\Delta\eta = 6/199$ in each case.

η at boundary	4.4623	4.975	5.457	6.000
$M_{\rm ADM}/m$ at boundary	0.9707069	0.9711462	0.9711768	0.9711788

η at boundary	6.482	6.965	7.477	7.960
$M_{\rm ADM}/m$ at boundary	0.9711984	0.9711807	0.9711821	0.9711829

$$D_a s^a + K_{ab} s^a s^b - {\rm tr}K = 0. \tag{B1}$$

On the initial slice the extrinsic curvature vanishes and (B1) reduces to the "minimal area" condition

$$D_a s^a = 0. \tag{B2}$$

In general we may parametrize a spatial two-surface in an axisymmetric spacetime by a parameter l as

$$\mathcal{S} = (\eta(l), \theta(l), \phi), \tag{B3}$$

where, in principle, η and θ are arbitrary (C^2) functions of l. However in this work we restrict our search to surfaces of the form

$$\mathcal{S} = (h(\theta), \theta, \phi) \tag{B4}$$

(this restriction is also made by Cook [34] and Cook and York [48]). This is not an unreasonable restriction since it is known (see the discussion in Sec. V) that the surface must be of spherical topology and so the required curve should have end points at $\theta = 0$ and $\theta = \pi/2$. The additional restriction embodied in (B4) is that the curve is single valued in its θ component. This should not be troublesome since a double valued curve would contain two "turn-around" points where one would suspect that the divergence of outgoing normals would tend to be larger, making it more difficult for such a surface to be trapped.

From (B4) we may compute the coordinate components of the tangent to the curve

$$t^a = \left(\frac{dh}{d\theta},\ 1,\ 0\right), \tag{B5}$$

and from the normalizations conditions

$$t^a s_a = 0, \quad s^a s_a = 1, \tag{B6}$$

compute

$$s^a = \frac{1}{\Psi^2 e^q \sqrt{1 + (h_{,\theta})^2}} (1, -h_{,\theta}, 0). \tag{B7}$$

Inserting this into Eq. (B2) yields

$$\frac{d^2h}{d\theta^2} + \frac{dh}{d\theta}\left[1 + \left(\frac{dh}{d\theta}\right)^2\right]\left(\frac{\partial q}{\partial \theta} + \frac{4}{\Psi}\frac{\partial \Psi}{\partial \theta} + \cot\theta\right)$$

$$- \left[1 + \left(\frac{dh}{d\theta}\right)^2\right]\left(\frac{\partial q}{\partial \eta} + \frac{4}{\Psi}\frac{\partial \Psi}{\partial \eta}\right) = 0. \tag{B8}$$

Axial and equatorial plane symmetry require

$$\left.\frac{dh}{d\theta}\right|_{\theta=0} = \left.\frac{dh}{d\theta}\right|_{\theta=\pi/2} = 0, \tag{B9}$$

and, using L'Hospital's rule, the equation at $\theta = 0$ reduces to

$$\frac{d^2h}{d\theta^2} - \frac{2}{\Psi}\frac{\partial \Psi}{\partial \eta} = 0, \tag{B10}$$

and at $\theta = \pi/2$ to

$$\frac{d^2h}{d\theta^2} - \frac{\partial q}{\partial \eta} - \frac{4}{\Psi}\frac{\partial \Psi}{\partial \eta} = 0. \tag{B11}$$

Equations (B8), (B10), and (B11) are solved by finite differencing $h(\theta)$ according to the usual centered second order differencing operators (A17) and (A18). This produces a set of n_θ coupled nonlinear algebraic equations for the solution $h(\theta)$. The equations are solved using the well-known Newton-Raphson root finding algorithm (Press *et al.* [58] or Cook [34]). The stopping criteria was that the maximum of the residual [defined to be the absolute value of the right-hand side of (B8), (B10), and (B11) over the grid] be less than 10^{-8}. In general the convergence of the method was quite good; one could expect a lessening of the maximum of the residual by a

TABLE IV. Areal radius of the grid edge as a function of a with $b = 2$ and $w = 1$. The grid size is 200×53 with the outermost zone at $\eta = 6$.

	a						
Areal radius	-1.0	-0.5	0	0.5	1.0	1.5	2.0
r/m	206.0	203.5	202.7	202.7	203.2	204.0	205.1
$r/M_{\rm ADM}$	48.60	114.7	202.7	198.2	134.4	87.97	60.78
$r/M_{\rm AH}$	82.57	141.7	202.7	258.9	305.2	338.4	356.8

TABLE V. Convergence of some of the characteristics of the apparent horizon for initial data set (-0.8, 0, 1). The Gaussian curvature (GC) is in units of m^{-2}. In each case the outermost grid point is located at $\eta = 6$.

Grid size	$h(0)$	$h(\pi/2)$	M_{AH} / M_{ADM}	C_p/C_e	GC ($\theta = 0$)	GC ($\theta = \pi/2$)
50 × 14	1.214855	1.184160	1.0003427	0.7750775	-0.003658277	0.03989346
100 × 27	1.210591	1.179164	0.9981326	0.7728590	-0.003896767	0.04020071
150 × 40	1.210102	1.178664	0.9977441	0.7726530	-0.003922605	0.04021569
200 × 53	1.209907	1.178445	0.9976104	0.7725616	-0.003933012	0.04022679
250 × 66	1.209814	1.178340	0.9975498	0.7725178	-0.003937938	0.04023202
300 × 79	1.209761	1.178279	0.9975154	0.7724921	-0.003940798	0.04023516
350 × 92	1.209732	1.178247	0.9974966	0.7724787	-0.003942297	0.04023680
400 × 105	1.209714	1.178227	0.9974833	0.7724701	-0.003943259	0.04023785

factor of between 2 and 10 per iteration for a typical initial data set. (This type of *linear* convergence is typical for the Newton-Raphson algorithm if the terms are evaluated numerically.) Typically less than ten, and usually around five, iterations were required to reach the stopping criteria. Of course, as is usual for this method, the initial guess for the solution had to be reasonably good. Choosing a surface too far out would make the method diverge and there were some initial data sets which had an analogue of the problem whereby the method encounters a local extremum and shoots off to infinity. Generally speaking, a guess within one η unit (typically 1/6 the size of the entire grid) was good enough.

In general $h(\theta)$ will not occur right on a radial grid point, instead falling somewhere in between them. An interpolation scheme is needed in computing the values of the metric and extrinsic curvature components and their derivatives at $h(\theta)$. Here we have used the monotonically constrained cubic spline algorithm of Hyman [59].

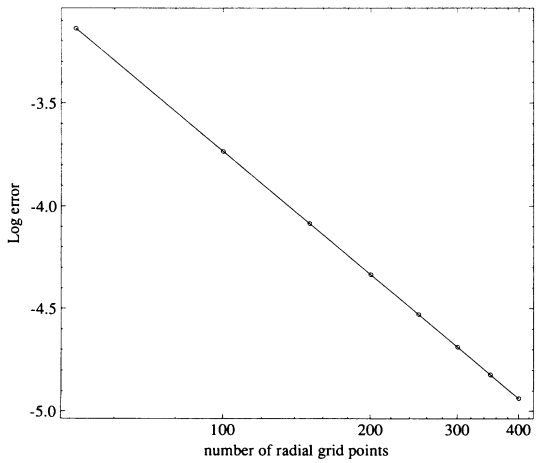

FIG. 16. Convergence of the maximum of the absolute value of the fourth order finite differenced residual of the trapped surface equation for the initial data set (-0.8, 0, 1). A least squares linear fit to the curve has slope -1.99. Run parameters are identical to Table V.

This interpolant has two advantages over the usual cubic splines: it is local and so should be computationally less strenuous, and it is constrained to appear smooth near discontinuities and sharp peaks. These considerations generally do not come into play on the initial slice. However during an evolution the equation (B1) has many more terms and it is sometimes desirable to solve it on every time slice and the computational savings may then be significant. Also it is known that in general one can expect the three-metric and extrinsic curvature components to form large second spatial derivatives during an evolution [19] and one would want the interpolant to be able to handle this case. The order of the spline is determined by the data out of which it is constructed. For reasonably smooth data the spline is constructed to be at least third order and in some cases fifth order. For not smooth data the order is in general less, though since the spline is local this applies only to the region in which the data is not smooth.

In any particular initial data set there may be multiple solutions to Eq. (B8). Even though one never knows exactly how many solutions there will be, inspection of the data and some prior geometrical experience (as with the Schwarzschild spacetime) usually was enough to convince that all solutions had been found.

We examine the initial data set (−0.8, 0, 1). Here the throat is an unstable minimal surface and the apparent horizon lies outside of the throat at about $\eta = 1.2$ (see Fig. 7). Table V shows the convergence of the following properties of the apparent horizon: its location on the axis and equator, mass, polar to equatorial circumference, and Gaussian curvature on the axis and equator. A rate of convergence may be found by using the same method as was used in the solution of the initial-value problem: the solution to the second order finite differenced system is fourth order differenced and then plugged back into the equation. The absolute value of the maximum of the residual is then used as an error measure. The data is shown in Fig. 16 and a least squares fit shows that the rate is nearly −2. This may be expected on the grounds that not only is the trapped surface condition finite differenced to second order but so is the Hamiltonian constraint, whose solution determines the geometry in which the apparent horizon is embedded.

[1] S. G. Hahn and R. W. Lindquist, Ann. Phys. (N.Y.) **29**, 304 (1964).
[2] A. A. Abramovici *et al.*, Science **256**, 325 (1992).
[3] A. Čadež, Ann. Phys. (N.Y.) **91**, 58 (1975).
[4] L. Smarr, Ann. N. Y. Acad. Sci. **302**, 569 (1977).
[5] K. Eppley, Ph.D. thesis, Princeton University, 1975.
[6] K. Eppley, Phys. Rev. D **16**, 1609 (1977).
[7] K. Eppley, in *Sources of Gravitational Radiation*, edited by L. Smarr (Cambridge University Press, Cambridge, England, 1979), p. 275.
[8] S. M. Miyama, Prog. Theor. Phys. **65**, 894 (1981).
[9] A. Abrahams, D. Bernstein, D. Hobill, E. Seidel, and L. Smarr, Phys. Rev. D **45**, 3544 (1992).
[10] P. Anninos, D. Bernstein, S. Brandt, D. Hobill, E. Seidel, and L. Smarr, this issue, Phys. Rev. D **50**, 3801 (1994).
[11] P. Anninos, D. Hobill, E. Seidel, L. Smarr, and W.-M. Suen (unpublished).
[12] P. A. Collins and R. M. Williams, Phys. Rev. D **5**, 1908 (1972).
[13] D. S. Brill, Ann. Phys. (N.Y.) **7**, 466 (1959).
[14] J. Wheeler, in *Relativity, Groups, and Topology*, Proceedings of the Summer School of Theoretical Physics, Les Houches, France, 1963, edited by C. DeWitt and B. DeWitt (Gordon and Breach, New York, 1964), pp. 316–520.
[15] A. Abrahams, Ph.D. thesis, University of Illinois, Urbana, Illinois, 1988.
[16] A. Abrahams and C. Evans, Phys. Rev. D **46**, R4117 (1992).
[17] J. York, in *Sources of Gravitational Radiation* [7].
[18] J. York, in *Frontiers in Numerical Relativity*, edited by C. Evans, L. Finn, and D. Hobill (Cambridge University Press, Cambridge, England, 1989).
[19] D. Bernstein, Ph.D. thesis, University of Illinois Urbana-Champaign, 1993.
[20] D. Bernstein and K.P. Tod, Phys. Rev. D **49**, 2808 (1994).
[21] A. Einstein and N. Rosen, Phys. Rev. **48**, 73 (1935).
[22] C. W. Misner, Ann. Phys. (N.Y.) **24**, 102 (1963).
[23] J. M. Bowen, Ann. Phys. (N.Y.) **165**, 17 (1985).
[24] R. Arnowitt, S. Deser, and C. W. Misner, in *Gravitation: An Introduction to Current Research*, edited by L. Witten (Wiley, New York, 1962).
[25] N. Ó Murchadha and J. York, Phys. Rev. D **10**, 2345 (1974).
[26] D. S. Brill and R. W. Lindquist, Phys. Rev. **131**, 471 (1963).
[27] M. Cantor and D. Brill, Compositio Mathematica **43**, 317 (1981). We thank Robert Bartnik for pointing out this reference to us.
[28] L. L. Smarr, Phys. Rev. D **7**, 289 (1973).
[29] J. M. Bardeen, *Black Holes* (Gordon and Breach, New York, 1973).
[30] A. Friedmann, Rev. Mod. Phys. **37**, 201 (1965).
[31] W. Israel, Can. J. Phys. **64**, 120 (1986).
[32] R. Penrose, Phys. Rev. Lett. **14**, 57 (1965).
[33] P. Anninos, D. Bernstein, S. Brandt, J. Libson, J. Massó, E. Seidel, L. Smarr, W.-M. Suen, and P. Walker (unpublished).
[34] G. Cook, Ph.D. thesis, University of North Carolina at Chapel Hill, Chapel Hill, North Carolina, 1990.
[35] G. Gibbons, Commun. Math. Phys. **27**, 87 (1972).
[36] S. W. Hawking, in *Black Holes*, edited by C. DeWitt and B. S. DeWitt (Gordon and Breach, New York, 1973).
[37] D. Christodoulou, Phys. Rev. Lett. **25**, 1596 (1970).
[38] R. Penrose, Ann. N.Y. Acad. Sci. **224**, 125 (1973).
[39] P. Jang and R. M. Wald, J. Math. Phys. **18**, 41 (1977).
[40] P. Anninos, Ph.D. thesis, Drexel University, 1989.
[41] J. W. York, Phys. Rev. Lett. **26**, 1656 (1971).
[42] A. Z. Petrov, *Einstein Spaces* (Pergamon, Oxford, England, 1969).
[43] L. Smarr, Ph.D. thesis, University of Texas, Austin, 1975.
[44] R. Penrose, Ann. Phys. (N.Y.) **10**, 171 (1960).
[45] L. Witten, Phys. Rev. **113**, 357 (1959).
[46] P. Szekeres, J. Math. Phys **6**, 1387 (1965).
[47] P. Anninos, D. Bernstein, D. Hobill, E. Seidel, L. Smarr, and J. Towns, *Numerical Astrophysics* (Springer-Verlag, New York, to be published).
[48] G. Cook and J. W. York, Phys. Rev. D **41**, 1077 (1990).
[49] K. Thorne, in *Magic Without Magic: John Archibald Wheeler*, edited by J. Klauder (Freeman, San Francisco, 1972), p. 231.
[50] E. Flanagan, Phys. Rev. D **44**, 2409 (1991).
[51] E. Flanagan, Phys. Rev. D **46**, 1429 (1992).
[52] D. Bernstein, D. Hobill, E. Seidel, J. Towns, and L. Smarr (unpublished).
[53] D. A. Anderson, J. C. Tannehill, and R. H. Pletcher, *Computational Fluid Mechanics and Heat Transfer* (Hemisphere, New York, 1984).
[54] A. Čadež, Ann. Phys. (N.Y.) **83**, 449 (1974).
[55] N. T. Bishop, Gen. Relativ. Gravit. **14**, 717 (1982).
[56] T. Nakamura, Y. Kojima, and K. Oohara, Phys. Lett. **106A**, 235 (1984).
[57] K. P. Tod, Class. Quantum Grav. **8**, L115 (1991).
[58] W. H. Press, B. P. Flannery, S. A. Teukolsky, and W. T. Vetterling, *Numerical Recipes* (Cambridge University Press, Cambridge, England, 1986).
[59] J. M. Hyman, SIAM J. Sci. Stat. Comput. **4**, 645 (1983).

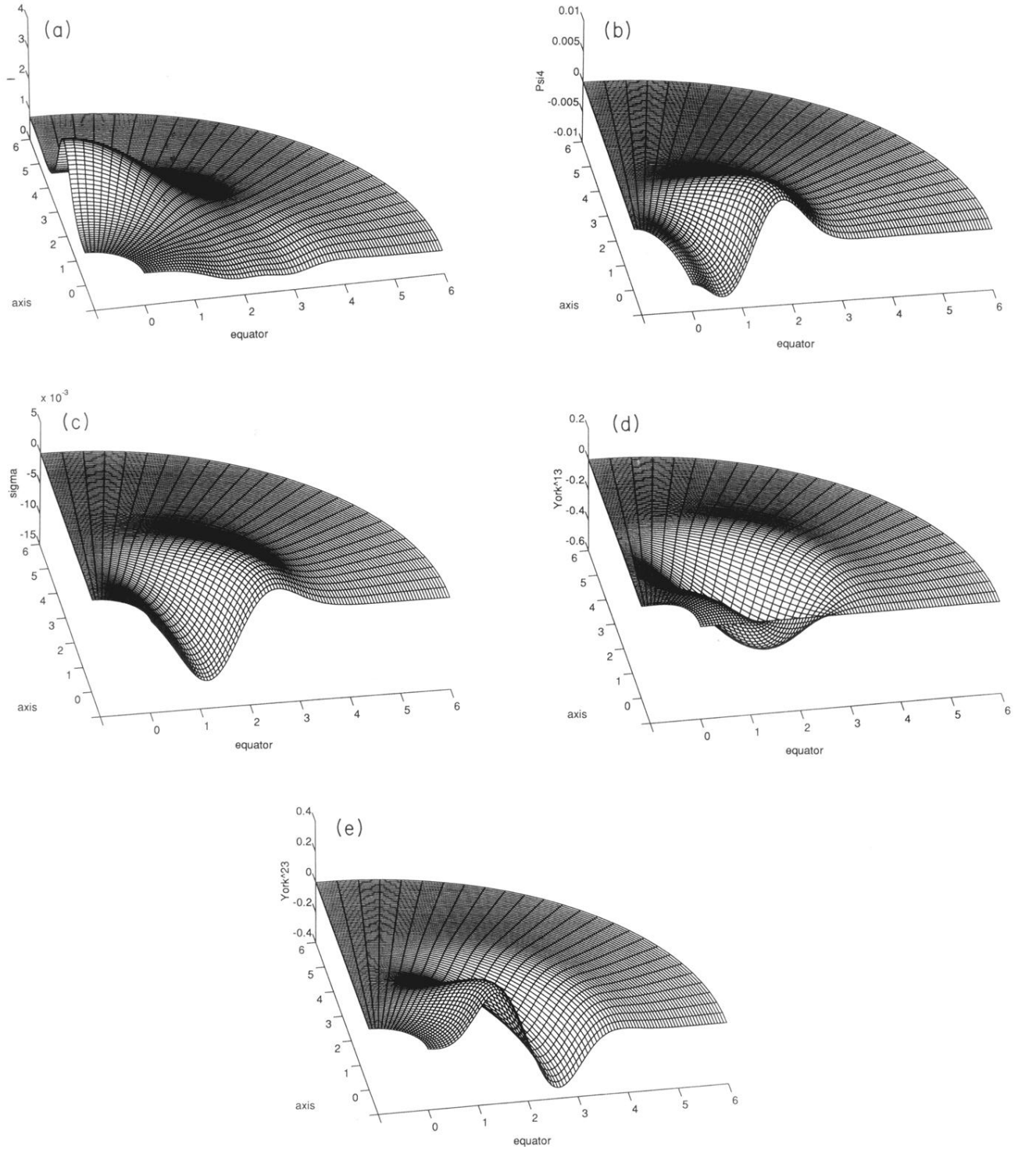

FIG. 12. Various curvature and radiative quantities plotted as a function of η and θ for the data set $a = 0.1$, $b = 2$, $w = 1$. (a) The curvature invariant I divided by the spherically symmetric value (36) using the areal radius of the constant η shell for r and the ADM mass for M. (b) Weyl tensor component Ψ_4, (c) spin coefficient σ, (d) York tensor component $\tilde{\beta}^{13}$, and (e) York tensor component $\tilde{\beta}^{23}$. Each quantity is in the appropriate units of the ADM mass. The grid size is 200×53 with outermost zone at $\eta = 6$ in all cases.

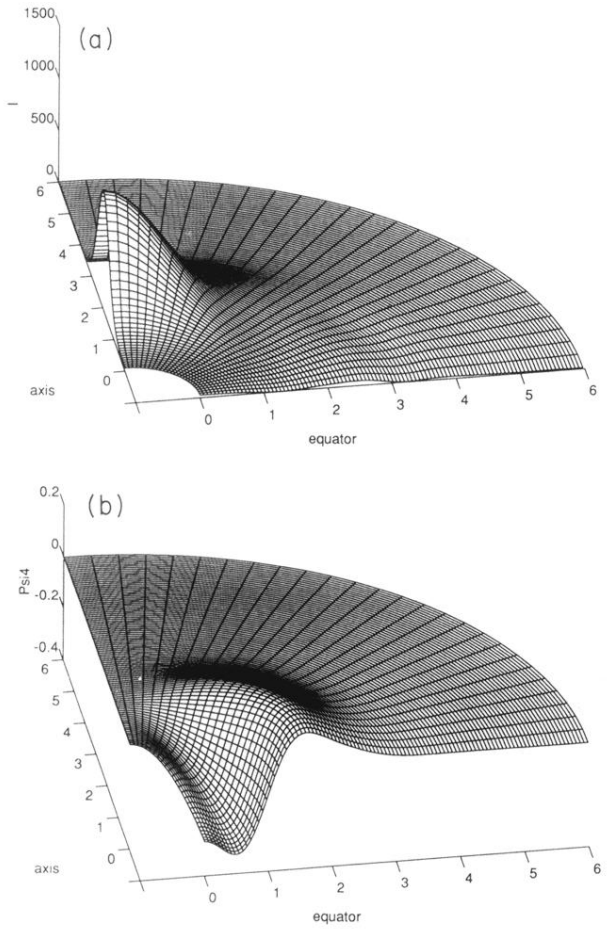

FIG. 13. (a) The curvature invariant I normalized to its spherically symmetric value for data set $a = 1$, $b = 2$, $w = 1$. (b) Weyl tensor component Ψ_4 for the same initial data set. Each quantity is in the appropriate units of the ADM mass. The grid size is 200×53 with outermost zone at $\eta = 6$ in all cases.

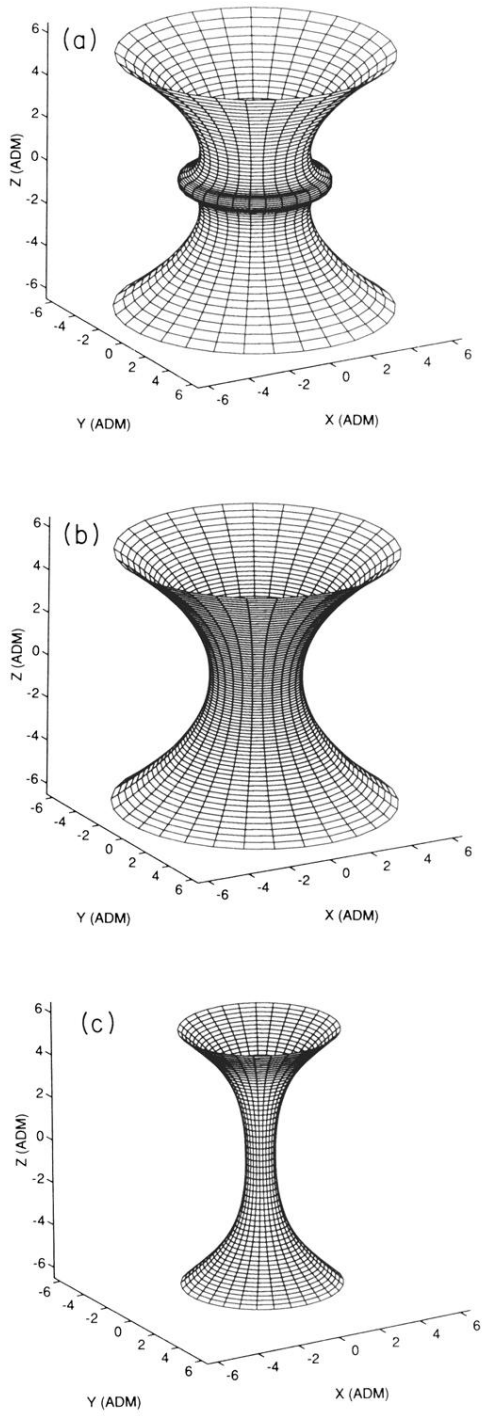

FIG. 6. Isometric embeddings of the equatorial plane for initial data sets $(a,\ 0,\ 1)$ with $a = -0.59$ (a), $a = 0$ (b), and $a = 1$ (c). The diagrams are each plotted out to proper distance $8M_{\mathrm{ADM}}$ (about $\eta = 2.7$ in each case) and the flat space coordinates are in units of the respective ADM masses. As the amplitude a becomes more negative, the geometry develops a shape akin to the classic "bag of gold."